



**HAL**  
open science

# Coseismic Underground Rupture, Geometry, Historical Surface Deformations and Seismic Potentials of the March 28, 2019 Mw 5.04 Mangya earthquake fault

Shengli Wang, Wujun Wu, Qinghong Li, Chao Li, Yongxiang Li, Yan Chen, Liangshu Wang, Mingjie Xu, Zhi Guo

► **To cite this version:**

Shengli Wang, Wujun Wu, Qinghong Li, Chao Li, Yongxiang Li, et al.. Coseismic Underground Rupture, Geometry, Historical Surface Deformations and Seismic Potentials of the March 28, 2019 Mw 5.04 Mangya earthquake fault. *Tectonics*, 2020, 39 (11), pp.e2020TC006244. 10.1029/2020TC006244 . insu-02977840v1

**HAL Id: insu-02977840**

**<https://insu.hal.science/insu-02977840v1>**

Submitted on 5 Jan 2021 (v1), last revised 22 Feb 2021 (v2)

**HAL** is a multi-disciplinary open access archive for the deposit and dissemination of scientific research documents, whether they are published or not. The documents may come from teaching and research institutions in France or abroad, or from public or private research centers.

L'archive ouverte pluridisciplinaire **HAL**, est destinée au dépôt et à la diffusion de documents scientifiques de niveau recherche, publiés ou non, émanant des établissements d'enseignement et de recherche français ou étrangers, des laboratoires publics ou privés.

1 **Coseismic Underground Rupture, Geometry, Historical Surface Deformations**  
2 **and Seismic Potentials of the March 28, 2019 *M<sub>w</sub>* 5.04 Mangya earthquake**  
3 **fault**

4 **Shengli Wang<sup>1\*</sup>, Wujun Wu<sup>1,2\*</sup>, Qinghong Li<sup>3</sup>, Chao Li<sup>1†</sup>, Yongxiang Li<sup>1</sup>, Yan**  
5 **Chen<sup>4</sup>, Liangshu Wang<sup>1</sup>, Mingjie Xu<sup>1</sup>, Zhi Guo<sup>5</sup>**

6 <sup>1</sup>School of Earth Sciences and Engineering, Nanjing University, Nanjing, China

7 <sup>2</sup>Key Laboratory of Reservoir Characterization, Research Institute of Petroleum  
8 Exploration and Development-Northwest, PetroChina, Lanzhou, China

9 <sup>3</sup>CNPC Xibu Drilling Engineering Company Limited, Urumqi, China

10 <sup>4</sup>Univ. Orléans, CNRS, BRGM, ISTO, UMR 7327, F-45071, Orléans, France

11 <sup>5</sup>Institute of Geology, China Earthquake Administration, Beijing, China

12 Corresponding author: ShengLi Wang ([wangsl@nju.edu.cn](mailto:wangsl@nju.edu.cn))

13 \*Shengli Wang and Wujun Wu contributed equally to the study and are co-first authors.

14 †Current address: School of Earth Sciences and Engineering, Hohai University, Nanjing,  
15 China

## 16 Abstract

17 The March 28, 2019  $M_w$  5.04 Mangya earthquake damaged eight ongoing drilling  
18 boreholes in the oil-production Yingxiong Ling (YXL) area, southwestern Qaidam of  
19 northern Tibet. The borehole damages provide an opportunity to measure directly the  
20 coseismic slips, the rupture area, and the seismic moment. The damages reveal the  
21 underground rupture area of  $45.30 \pm 10.24 \text{ km}^2$ , the maximum slip of  $400 \pm 13 \text{ mm}$ , and  
22 the seismogenic fault dip of  $\sim 38.6^\circ$ . These parameters generate a seismic moment of  
23  $(1.81 \pm 0.47) \times 10^{17} \text{ Nm}$  and a moment magnitude of  $5.47 \pm 0.16$ . Seismic exploration  
24 reveals that the geometry of the SZG ramp, the uppermost part of the multi-bend  
25 Yingxiong Ling thrust system, agrees primarily with the rupture plane derived from the  
26 borehole damages and one plane of the focal mechanism solution. This suggests that this  
27 earthquake resulted from slipping on the ramp. The hanging wall of the YXL thrust  
28 system forms the complex fault-bend fold YXL anticlinorium. Active thrusting and  
29 folding along both edges of YXL attest to the southwestern vergence of this thrust  
30 system. Growth strata demonstrate average slip rates of the thrust system ranging from  
31  $\sim 0.2 \text{ mm/yr}$  to  $\sim 0.3 \text{ mm/yr}$ . The thrust and folded recent alluviums along the  
32 southwestern edge indicate two thrusting events with coseismic slips of  $1.7 \pm 0.15 \text{ m}$  and  
33  $3.5 \pm 0.15 \text{ m}$  at  $6.16 \pm 0.52 \text{ ka}$  and  $\sim 35.91 \text{ ka}$ , respectively. The entire rupturing of the  
34 thrust system can produce  $M_w 7.65 \pm 0.03$  earthquakes.

35 Keywords: the March 28, 2019  $M_w$  5.04 Mangya earthquake; coseismic rupture; seismic  
36 potential; Yingxiong Ling; Qaidam; Tibet

## 37 1 Introduction

38 Earthquakes occur due to sudden shear slip on faults within the Earth. Although  
39 some geophysical, geodetic (e.g., [Feng et al., 2010](#); [Xu et al., 2010](#)) and morphotectonic  
40 techniques (e.g. [Xu et al., 2009](#); [Liu-Zeng et al., 2009](#)) are available to estimate coseismic  
41 slips and rupture areas, precisely quantifying coseismic slips without surface ruptures  
42 occurring in a several-second time scale remains a grand challenge, particularly for  
43 addressing issues, such as fault propagation, fault interaction, and assessing the moment  
44 magnitude. Under certain favorable circumstances, coseismic slips may be recorded by  
45 offsets of features that penetrate a fault plane, including geomorphic markers and/or  
46 artificial structures. However, these circumstances are scarce.

47 Here, we describe a case example that the coseismic rupture of the March 28,  
48 2019 Mangya earthquake fault in southwestern Qaidam, northern Tibet ([Figure 1](#)) can be  
49 retrieved by quantifying damages of eight ongoing drilling boreholes and drilling tools.  
50 With the records of this event, we determine the coseismic slip and rupture area of the  
51 earthquake fault. Also, we present three seismic profiles to analyze the geometry, seismic  
52 potentials, and the long-term slip rates of the earthquake fault.

## 53 2 Geological Setting

54 The Himalayan-Tibetan orogen went through subduction mountain building,  
55 terrane accretion until present continent-continent collisional mountain building (e.g.,  
56 [Yin and Harrison, 2000](#)). Persistent Indian indentation into Eurasia resulted in the growth  
57 of the Tibetan plateau (e.g., [Tapponnier et al., 2001](#); [Zuza et al., 2019](#)), large-scale

58 shortening in central Asia (Molar and Tapponnier, 1975; Tapponnier and Molar, 1979;  
59 Chen et al., 1993) and extrusion of East and Southeast Asia (Tapponnier and Molnar,  
60 1976; 1977; Tapponnier et al., 1982). The western Kunlun range, the Altyn Tagh fault  
61 and the Qilian range initiated to form the northern edge of the Tibetan plateau shortly  
62 after the Indo-Tibetan collision (e.g., Yin et al., 2002; 2008a; Pang et al., 2019; Zuza et  
63 al., 2019; Chen et al., 2002), and persist presently (e.g., Wang et al., 2017a). The Qaidam  
64 Basin, the largest active hinterland one with an average elevation of ~3000 m in northern  
65 Tibet, is bounded by the Altyn Tagh fault in the northwest, the Qilian Shan in the  
66 northeast, and the Eastern Kunlun in the south (Figure 1b), and elevated by sediments  
67 infilling (e.g., Tapponnier et al., 2001; Wang et al., 2014). NW–NWW trending folds are  
68 widespread all over Qaidam (e.g., Qinghai BGMR, 1991; Zhou et al., 2006; Yin et al.,  
69 2007; 2008a; 2008b; Chen et al., 2010; Wu et al., 2013; Pan et al., 2015; Cheng et al.,  
70 2018).

71 Yingxiong Ling (YXL) is an active NW-trending anticlinorium with its highest  
72 peak of ~3835 m in southwestern Qaidam (Figure 1a), consisting of the Shizigou-Yousha  
73 Shan (SZG-YSS) anticline in the southwest, the Ganchaigou (GCG) anticline in the  
74 middle, and the Xianshuiquan-Youquanzi (XSQ-YQZ) anticline in the northeast (Figure  
75 1a; Yin et al., 2007; Yu et al., 2011; Pan et al., 2015; Cheng et al., 2018; Huang et al.,  
76 2018; Bian et al., 2019; Wu et al., 2020).

77 Cenozoic stratigraphic divisions and age assignments of southwestern Qaidam are  
78 based on terrestrial fossils (e.g., spores, ostracods, and pollen) found in outcrop sections,  
79 magnetostratigraphy, fission-track, detrital  $^{40}\text{Ar}/^{39}\text{Ar}$  dating, and the basin-wide  
80 stratigraphic correlation of outcrop geology and drill cores with seismic profiles (Huo,  
81 1990; Qinghai B.G.M.R., 1991; Yang et al., 1992; Song and Wang, 1993; Huang et al.,  
82 1996; Xia et al., 2001; Qiu, 2002; Sun et al., 2005; Rieser et al., 2006a, 2006b; Chang et  
83 al., 2015; Wang et al., 2017; Cheng et al., 2019). Major Cenozoic stratigraphic units  
84 include the Lulehe ( $E_{1-2l}$ ), the lower ( $E_3^1xg$ ) and upper ( $E_3^2xg$ ) members of the  
85 Xiaganchaigou, the Shangganchaigou ( $N_{1sg}$ ), the Xiayousha Shan ( $N_2^1sy$ ), the  
86 Shangyousha Shan ( $N_2^2sy$ ), the Shizigou ( $N_2^3s$ ), and the Qigequan ( $Q_{1q}$ ) Formations. We  
87 refer to Bian et al.'s (2019) summary for the Cenozoic stratigraphy of the YXL region  
88 (Table 1).

89 Before the March 28, 2019 Mw 5.04 Mangya earthquake occurred in YXL,  
90 southwestern Qaidam of northern Tibet (Figure 1b; USGS, 2019; China Earthquake Data  
91 Center, 2019), the January 2, 1977 Mw 6.4 and Mw 5.1, and the February 26, 1987 M 6.1  
92 earthquakes were recorded in this region (Wang et al., 1999). Since the Qaidam Basin is  
93 the largest hydrocarbon-bearing hinterland sedimentary basin in the Tibetan Plateau  
94 (Horton et al., 2012), high-quality and high-resolution exploration seismic data have been  
95 achieved to explore the deep structural trap in this area (e.g., Yin et al., 2007; 2008a; 2008b;  
96 Chen et al., 2010; Wu et al., 2013; Pan et al., 2015; Bian et al., 2019; Wu et al., 2020).  
97 Active folding and thrusting deformed recent alluviums and abandoned geographic  
98 markers along the southwestern edges of YXL (Xu et al., 2018a; 2018b). Moreover, as  
99 the epicenter of this event at YXL is located in the mature oil-production region,  
100 exploration and development of hydrocarbon offer numerous high-quality seismic data  
101 and well logs with on-going drilling boreholes, and provide a solid base for addressing  
102 these issues.

### 103 3 The coseismic underground slips of the March 28, 2019 Mangya earthquake fault

104 Dense boreholes have been drilled in the zone of YXL where locates the epicenter  
105 of the March 28, 2019 Mw 5.04 Mangya earthquake (Figures 1b and 2); eight ongoing  
106 drilled boreholes were directly damaged by the coseismic underground slip of the  
107 earthquake fault. They are namely H4-3-414, H4-3-510, H4, H6-2-510, H4-2-506, H2-3-  
108 413, H4-3-411, and H4-2-510 (Figure 2). The damage types include bit freezing and  
109 cutting of drilling rods and casing pipes.

#### 110 3.1 Slip at borehole H4-3-414

111 Drilling of borehole H4-3-414 was finished on March 25, 2019. When the  
112 instruments of transmission logging were intruding to the depth of ~2590 m at 5:36, the  
113 earthquake happened. The drilling rods were stuck on the mainshock and could not be  
114 moved. An aftershock occurred at 7:20. After releasing stuck and pulling out, the drilling  
115 rod was broken off (Figures 3a and b) and the logging tools fell into the hole. The kink-  
116 like bend and breaking-off of the drilling pipe (Figures 3a and b) indicate that it was  
117 sheared to break off completely by a low-angle thrust. A 165-mm-diameter lead seal was  
118 put into the hole and was stuck at the depth of ~2034.79 m, and then was pulled out. Its  
119 side face has scratches (Figure 4c), demonstrating that the lead seal passed by the upper  
120 fracture of the 196.8-mm-diameter casing pipe when the lead seal was put into and/or  
121 pulled out from the hole through the cutoff of the casing pipe. And the bottom of the lead  
122 seal is clear (Figure 4d), indicating that it did not touch the lower fracture of the casing  
123 pipe, and the casing pipe was sheared to break off completely at the depth of ~2034.79 m.  
124 Therefore, the offset of the casing pipe is more than its outer diameter of 196.85 mm.  
125 Assuming that the kink-like deformation of the drilling rod is symmetrical with respect to  
126 the broken surface and the rod is just broken away (Figures 3c–g), the offset is  $400 \pm 13$   
127 mm (Figure 3g) in the scenario of the sum of the kink-like width of  $250 \pm 13$  mm (Figure  
128 3g), and the difference of 149.87 mm (Figure 3f) between the inner diameter (166.63  
129 mm) of the casing pipe and the double drilling rod wall thickness (16.76 mm). The error  
130 results from the rugged fracture surface of the broken drilling pipe.

#### 131 3.2 Slip at borehole H4-3-510

132 Borehole H4-3-510 was being drilled to the depth of ~4323 m when the  
133 earthquake happened. The suspending weight of the drilling rods and tools was ~850 KN  
134 before the earthquake, increased suddenly to ~1700 KN on the shock, and then decreased  
135 to ~400 KN after the shock. The pressure of the pump for drilling fluid circulation  
136 decreased to null and the loss of circulation occurred after the shock, indicating that the  
137 drilling fluid leaked to break off the return of the circulation, and that the casing pipe was  
138 severely broken. After the shock, the suspending weight of the uplifting drilling rods and  
139 tools of ~400 kN demonstrates that parts of the drilling rods and tools were disjointed.  
140 Two make-ups did not work, and so the drilling rods and tools were not connected. The  
141 drilling rods and tools pulled out from the hole is ~2110.47 m long, so the fish of the  
142 drilling rods and tools assemblage kept in the borehole is ~2212.53 m in length. The  
143 cutting surface of the uplifted drilling rod reveals that the intermediate casing strings  
144 were sheared off by the coseismic slip of the earthquake fault at the depth of ~2110.47 m  
145 to result in leaving the fish in the borehole. Therefore, we deduce that the offset of the

146 drilling rod is more than the diameter of the intermediate casing strings of 196.85 mm.  
147 The damage of borehole H4-3-510 is identical to that of borehole H4-3-414 in the  
148 scenario of [Figures 3f](#) and [g](#).

### 149 3.3 Slip at borehole H4

150 When borehole H4 was being drilled to the depth of ~4417.17 m, the earthquake  
151 happened. On pulling up the drilling rods and tools, its suspending weight increased from  
152 ~940 KN to ~1000 KN, implying that a part of the drilling rods was stuck, but not broken  
153 off. About 9 m<sup>3</sup> of drilling fluid with a density of 1.98 g/cm<sup>3</sup> leaked, revealing that a  
154 casing pipe was squeezed to break and to stick a drilling rod. The depth of the drilling rod  
155 sticking is ~1700 m, determined from pulling drilling rods up. The drilling rod sticking  
156 indicates that the offset of the casing pipe is no more than 149.87 mm, the difference  
157 between the inner diameter (166.63 mm) of the casing pipe and the double-wall thickness  
158 (16.76 mm) of a drilling rod, as the drilling rod is completely squashed ([Figure 3f](#)), and is  
159 no less than the difference of 65.03 mm between the inner diameter of the casing pipe and  
160 the outer diameter (101.60 mm) of the drilling rod, as both sides of the drilling rod just  
161 touches the casing pipe ([Figure 3e](#)). Therefore, the coseismic displacement at this  
162 borehole is  $107 \pm 42$  mm.

### 163 3.4 Slip at borehole H6-2-510

164 When a loss of circulation of borehole H6-2-510 was being handled, the  
165 earthquake occurred. After the main shock, naked drilling rods were put into the borehole  
166 and got tight at the depth of ~1994.74 m, implying that the casing pipe was severely  
167 deformed at that depth. Its offset is more than the difference of 108.21 mm between the  
168 inner diameter (247.91 mm) of the intermediate casing string and the outer diameter  
169 (139.70 mm) of the drill rod sub, similar to the scenario of [Figure 3e](#), which is the  
170 minimum amount of deformation. However, the deformed borehole was made a wiper  
171 trip by processing milling taper and casing milling, indicating that the diameter of the  
172 deformed intermediate casing string at the depth is more than the minimum diameter (124  
173 mm) and less than the maximum (240 mm) of the milling taper. Thus, the coseismic  
174 displacement at this site is  $182 \pm 58$  mm. The borehole logging ([Table 2](#)) shows  
175 deformations from the depth of 1970 m to 1990 m. The amount of deformation is  
176 significantly less than what we deduced at the depth of ~1994.74 m.

### 177 3.5 Slip at borehole H4-2-506

178 When a loss of drilling fluid circulation of borehole H4-2-506 was being handled,  
179 the earthquake occurred. After the main shock, naked drilling rods were put into the  
180 borehole to the depth of 3674 m and then were pulled up to the depth of 1000 m on  
181 March 28, indicating that the coseismic deformation of the borehole is significantly less  
182 than the difference of 79.61 mm between the diameter (168.3 mm) of the drilling pipe sub  
183 and the inner diameter (247.91 mm) of the intermediate casing string. However, a 241.3-  
184 mm-diameter drill bit was put into the borehole and got tight at the depth of ~1925 mm  
185 on March 31, demonstrating that the casing pipe was squeezed. Its offset should be more  
186 than the difference of 6.61 mm between the inner diameter (247.91 mm) of the  
187 intermediate casing string and the diameter (241.30 mm) of the drill bit, which is the  
188 minimum amount of deformation. The borehole logging ([Table 2](#)) shows that the

189 maximum is 48.40 mm. Therefore, the total offset of the borehole is more than 6.61 mm  
190 and less 48.40 mm at the depth of ~1925 m, this is to say that the slip at this borehole site  
191 is  $28 \pm 21$  mm.

### 192 3.6 Slip at borehole H2-3-413

193 The coseismic slip of the Mangya earthquake fault deformed the casing pipe of  
194 borehole H2-3-413 to stick the drilling rod at the depth of ~1500.0 m when the drilling  
195 rods were being pulled up after the borehole inclination had been measured. The borehole  
196 had been drilled to the depth of ~1899 m. The coseismic drilling pipe sticking indicates  
197 that the slip at this site is no less than the difference of 128.27 mm between the inner  
198 diameter (255.27 mm) of the casing pipe and the outer diameter (127 mm) of the drilling  
199 rod, as both sides of the drilling rod just touched the casing pipe (similar to the situation  
200 of [Figure 3e](#)), and no more than 236.89 mm, the difference between the inner diameter of  
201 the casing pipe and the double-wall thickness (18.38 mm) of the drilling rod, as the  
202 drilling pipe was completely squashed (similar to the situation of [Figure 3f](#)). Therefore,  
203 the coseismic displacement at this site is  $188 \pm 59$  mm.

### 204 3.7 Slip at borehole H4-3-411

205 The Mangya earthquake happened when borehole H4-3-411 was being drilled to  
206 the depth of ~2159 m. The coseismic slip of the earthquake fault deformed the casing  
207 pipe to stick the drilling rod. However, the sticking depth was weakly constrained. The  
208 sticking was not released by many methods, indicating that the deformation of casing  
209 pipes and drilling rods of borehole H4-3-411 are identical to those of borehole H2-3-413.  
210 So, the coseismic slip at the borehole site is  $188 \pm 59$  mm.

### 211 3.8 Slip at borehole H4-2-510

212 The mainshock occurred when boreholes H4-2-510 was being drilled to the depth  
213 of 4828 m. Just after the main shock, it was found that drilling pipes got stuck, indicating  
214 the coseismic deformation of the borehole. The stuck depth was measured at ~2271 m by  
215 pulling up drilling rods. The sticking of the drilling rods indicates that the casing pipe at  
216 the stuck depth was squeezed to extrude the drilling rod at that depth. As the drilling rod  
217 was completely pressed to flat (the situation of [Figure 3f](#)), the offset of the borehole at the  
218 stuck depth is 149.87 mm, the difference between the inner diameter (166.63 mm) of the  
219 casing pipe and the double-wall thickness (16.76 mm) of the drilling rod. As both sides of  
220 the drilling rod just touched the casing pipe (the situation of [Figure 3e](#)), the offset is the  
221 difference of 65.03 mm between the inner diameter of the casing pipe and the outer  
222 diameter (101.60 mm) of the drilling pipe. So, the coseismic displacement at this  
223 borehole site is  $107 \pm 42$  mm.

### 224 3.9 Coseismic underground rupture area

225 Boreholes H4-3-510 and H4-3-411 have the maximum offsets. The amount of  
226 offsets decreases northwestwards and southwestwards from these two boreholes. In the  
227 northeast and southeast of them, coseismic slips are not well constrained due to the lack  
228 of ongoing drilling wells. Nonetheless, we may assume that the coseismic slips decrease  
229 radially and linearly with distances away from the point of the maximum slip. The

230 coseismic slips at the eight boreholes indicate that the maximum slip of  $400 \pm 13$  mm  
231 locates proximately at the center between boreholes H4-3-510 and H4-3-414. Using  
232 linear interpolation and extrapolation, we fit a contour map of coseismic slips (Figure 2).  
233 The fitted contour map presents an ellipse shape with a half long axis of  $4.01 \pm 0.45$  km  
234 and a half short axis of  $2.81 \pm 0.32$  km.

235 An ellipse area is defined as

$$236 \quad \quad \quad ARA = \pi a b \quad \quad \quad (1)$$

237 where  $a$  is the half length of the long axis,  $b$  is the half length of the short axis, and  $ARA$   
238 is the area of the projected ellipse. The projected area of the coseismic rupture of  $35.40 \pm$   
239  $8.00$  km<sup>2</sup> is therefore obtained.

240 These eight damaged boreholes reveal their coseismic slips on the earthquake  
241 fault plane and rupture depths (Table 3). Boreholes H4-3-414, H4-3-510, H4, H6-2-510,  
242 and H4-2-506 were drilled by PertoChina; their construction records and earthquake  
243 damages are detailed, precise, and reliable. However, boreholes H2-3-413, H4-3-411, and  
244 H4-2-510 were outsourced; their construction records and earthquake damages are rather  
245 simple, less precise and undependable; but their locations and damages are reliable. Thus,  
246 we use the parameters of the first five boreholes to fit a plane. The plane formulae is

$$247 \quad \quad \quad z = -0.336x - 0.726y + 13274438.528 \quad \quad \quad (2)$$

248 with a dip angle of  $38.6^\circ$ . This dip is slightly contrast to the attitude of plane 1  
249 determined from the focal mechanism solution of the Mangya earthquake (Table 4).

250 Therefore, the true rupture area is given as

$$251 \quad \quad \quad RA = ARA / \cos \alpha \quad \quad \quad (3)$$

252 where  $RA$  is the true rupture area,  $ARA$  is the area of projected ellipse, and  $\alpha$  is the dip  
253 angle of the fault plane. Using the fitted dip angel, the projected area, and formula (3), the  
254 true underground coseismic rupture area of  $45.30 \pm 10.24$  km<sup>2</sup> can be generated. This  
255 value may be a lower limit of the Mangya earthquake fault rupture since the eight  
256 boreholes are primarily located in the western part of the deductive rupture area.

### 257 3.10 The measured seismic moment and the moment magnitude

258 Damages of the boreholes reveal the true coseismic rupture area and slips. The  
259 moment magnitude can be thus determined by the relations

$$260 \quad \quad \quad M_0 = \mu A S \quad \quad \quad (4)$$

261 where  $M_0$  is the seismic moment,  $\mu$  is the shear modulus,  $A$  is the faulted area, and  $S$  is the  
262 average slip over the faulted area, and

$$263 \quad \quad \quad M_w = 2/3 \log M_0 - 6.03 \quad \quad \quad (5)$$

264 where  $M_w$  is the moment magnitude. Adopting the measured faulted area for  $A$ , the  
265 coseismic slips for  $S$  decreasing radially and linearly away from the maximum point, and  
266 the shear modulus of  $30 \times 10^9$  N/m<sup>2</sup>,  $M_0$  of  $(1.81 \pm 0.47) \times 10^{17}$  Nm and  $M_w$  of  $5.47 \pm 0.16$   
267 can be produced.



## 268 **4 Geometries of the YXL anticlinorium and the YXL thrust system**

269 We present three seismic profiles in [Figures 5, 6 and 7](#) to decipher the geometries  
270 of the March 28, 2019 Mangya earthquake fault and the YXL anticlinorium. These  
271 seismic profiles image a sub-horizontal reflector, crossing other inclined reflectors  
272 ([Figures 5, 6 and 7](#)) at their uppermost parts. Drilling and well logging reveal that this  
273 sub-horizontal reflector presents the groundwater level. [Figure 5](#) shows the geometry of  
274 the entire middle YXL anticlinorium. [Figure 6](#) approximately crosses perpendicularly the  
275 northwestern SZG-YSS anticline near the coseismic rupture region of the Mangya  
276 earthquake fault ([Figures 1 and 2](#)). [Figure 7](#) crosses the southeastern SZG-YSS anticline.  
277 Formation boundaries in these seismic profiles are defined based on fossils from drilling  
278 cores, lithology and synthetic seismogram, and therefore correlate to seismic reflectors.  
279 According to characteristics of the seismic reflector assemblage, formation boundaries  
280 are extrapolated to neighboring profiles. We invoke the fault-related folding theories  
281 ([Suppe, 1983](#); [Suppe and Medwedeeff, 1990](#); [Medwedeeff and Suppe, 1997](#)), growth strata  
282 theory ([Suppe et al., 1992](#)) and the kink method to interpret these seismic profiles in finer  
283 scales to decipher the geometries of the YXL anticlinorium and the YXL thrust system.

### 284 4.1 The YXL anticlinorium

285 We interpret YXL as a complex fault-bend fold anticlinorium, produced by the  
286 southwest-vergent thrusting of the YXL thrust system ([Figures 5a and b](#)). The  
287 northwestern SZG-YSS anticline is made up of a breakthrough fault-propagation fold  
288 anticline on surface and a wedge structure in depth ([Figures 5b and 6b](#)), and the  
289 southeastern SZG-YSS anticline ([Figure 7a and b](#)) is a forelimb breakthrough fault-  
290 propagation fold anticline (see Appendix A for a complete description).

291 The kink-band width of  $3.5 \pm 0.2$  km between the axial surfaces A and A' ([Figure](#)  
292 [6b](#)) reveals the slip along the lower SZG ramp in the northwestern SZG-YSS anticline.  
293 The bottom age of the growth strata in the northeast limb of the northwestern SZG-YSS  
294 anticline is interpolated at  $17.2 \pm 1.0$  Ma based on the thickness ([Figure 6b](#)), with the  
295 ages of  $\sim 15.3$  Ma and  $\sim 22.0$  Ma for the top and bottom of the Xiayousha Shan Formation,  
296 respectively ([Bian et al., 2019](#)). These parameters produce an average slip rate of  $\sim 0.2$   
297 mm/yr for the lower SZG ramp.

298 The kink width between the axial surfaces A'' and A in the southeastern SZG-YSS  
299 anticline stands for a slip of  $\sim 4.67$  km along the YSS ramp ([Figure 7b](#)). Using the ages of  
300 the top and bottom of the Xiayousha Shan Formation, the basal age of the growth strata is  
301 interpolated at  $16.5 \pm 1.0$  Ma which is slightly younger than that of the northwestern  
302 segment of the anticline. These parameters produce an average slip rate of 0.3 mm/yr for  
303 the SZG ramp, which is slightly higher than that of the lower SZG ramp.

304 We interpret the GCG ridge as a classic fault-bend fold anticline based on locating  
305 regions of homogeneous dip (see Appendix B for a complete description; [Figures 5a and](#)  
306 [b](#)), and XSQ-YQZ as a multi-bend fault-bend fold anticline (see Appendix C for a  
307 complete description; [Figures 5a and b](#)).

## 308 4.2 The YXL thrust system

309 Detailed structural interpretation and analysis indicate that the YXL anticlinorium  
310 is generated by the southwest-vergent thrusting of the multi-bend faults, namely the YXL  
311 thrust system (Figure 5b). The YXL thrust system in the northwestern YXL anticlinorium  
312 consists of the SZG ramp, the SZG back-ramp, the SZG flat, the lower SZG ramp, the  
313 GCG ramp, the XSQ flat, the upper XSQ ramp, the lower XSQ ramp, and the lower XSQ  
314 flat (Figures 5b and 6b). The thrust fault system, generating the SZG-YSS anticline,  
315 changes as the YSS ramp and the YSS flat (Figure 7b) in the southeastern YXL  
316 anticlinorium, with the SZG back-ramp waning.

317 The northwestern SZG-YSS comprises two stacked anticlines (Figures 5b and  
318 6b). The outcropping one is a forelimb breakthrough fault-propagation fold anticline with  
319 the high-angle or overturned forelimb (Figures 8 and 9) and the sub-horizontal crest  
320 (Figure 8); and the buried lower SZG wedge structure is a fault-bend fold anticline  
321 (Figures 5b and 6b), which is considered as the main hydrocarbon production trap in the  
322 YXL region. According to the fault-bend folding theory (Suppe, 1983), the width of  
323 ~3.48 km of the back-limb (the kind-band between the axial surfaces A and A') of the  
324 lower SZG anticline (Figure 6b) is equal to the slip along the lower SZG ramp. Figure 6b  
325 shows that the hanging wall ramp width is ~3.70 km, approximately matching the  
326 prediction of the classic fault-bend folding theory (Suppe, 1983).

327 The length of ~4.96 km of the forelimb along the fault and the back limb kink  
328 width of 5.42 km of the GCG anticline (Figure 6b) correspond to the slips before and  
329 after folding, respectively, approximately complying with the fault-bend folding theory  
330 (Suppe, 1983). However, the slip transferred forward from the GCG flat is significantly  
331 larger than the back limb kink width of northwestern SZG-YSS. The excess slip should  
332 be accommodated by the growth of the surface fault-propagation fold and movement  
333 along the break-through thrust ramp (Figures 5b and 6b).

334 The slip along the XSQ flat, the upper and the lower XSQ ramps can be obtained  
335 by the displacement of ~4.56 km of the bottom of the Lulehe Formation, which is slightly  
336 less than the slip of ~5.42 km along the GCG flat. This discrepancy probably results from  
337 the estimate of the length of the lower XSQ ramp and the bias in the time-depth  
338 conversion of the seismic profile.

## 339 4.3 The Shaxi wedge structure

340 The seismic profiles image well the Shaxi wedge structure (Figures 5 and 6),  
341 southwest of YXL. We interpret Shaxi as a wedge structure resulting from a northeast-  
342 vergent displacement of the thrust sheet to fold the strata above it to form a monocline  
343 based on locating regions of homogeneous dip and axial surfaces (see Appendix D for a  
344 complete description; Figures 5b and 6b). The growth axial surface G<sub>s</sub> and the active  
345 axial surface M terminate in the middle part of the Shangyousha Shan Formation (Figures  
346 5b and 6b), indicating its inactivity after deposition of this layer. This interpretation  
347 demonstrates that the width of ~3.57 km of the kind band between M and M' (Figures 5b  
348 and 6b) represents the slip of the thrust. We interpolate the top and bottom ages of the  
349 growth strata at ~10.4 Ma and ~36.8 Ma, respectively, according to the top and bottom  
350 depths of the growth strata in Figure 6 and the formation boundary ages (Bian et al.,

351 2019). These parameters produce an average slip rate of ~0.13 mm/yr of the blind thrust.  
352 The seismic profiles (Figures 5b and 6b) show that the Shaxi structure and the YXL  
353 structures have no kinematic links.

## 354 **5 Surface deformations resulting from activity of the YXL thrust system**

355 The borehole deformations and historical earthquakes (Wang et al., 1999) reveal  
356 that the multi-bend YXL thrust system is active. The hanging wall of the thrust system  
357 penetrates through active axial surfaces to fold inevitably recent alluviums and  
358 abandoned geomorphic markers (Suppe, 1983; Suppe et al., 1992; 1997). We observed  
359 that recent alluviums and geomorphic markers are folded and cut along both edges of  
360 YXL during our reconnaissance in the summer of 2019.

### 361 5.1 Active thrusting and folding along the southwestern edge of YXL

362 Fine-scale analysis of seismic profiles reveals that the traces of the SZG ramp and  
363 the active axial surface B' constitute the southwestern edge of northwestern YXL (Figures  
364 5b and 6b). The SZG ramp trace marks the southwestern surface border of northwestern  
365 YXL; the mountainous northwestern SZG-YSS anticline locates in its northeast; and  
366 there exists the desert covered by recent alluviums (Figure 8) in its southwest. The active  
367 axial surface B' denotes the underground southwestern border of northwestern YXL  
368 (Figures 5b and 6b).

#### 369 5.1.1 Active thrusting

370 The SZG ramp breaks through the southwestern limb of northwestern SZG-YSS  
371 and thrusts to the ground surface (Figures 1, 5b, 6b, 8, and 9; Xu et al., 2018a; 2018b).  
372 The modified river-cut section (Figures 9a and b) shows that the SZG ramp displaces the  
373 Qigequan Formation and recent alluviums. Unit A is folded and truncated by F3 (Figure  
374 9b). The southwestern part of the fold in Unit A is partially eroded; and Unit B laps on  
375 the erosional surface (Figure 9b). Folding of Unit A implies a thrusting event. The middle  
376 and lower parts of Unit B1 are truncated by F3; its upper part is folded to form an  
377 anticline. F3 refracts to a lower angle at a higher level and vanishes in the middle part of  
378 Unit B1. The top of folded Unit B1 is eroded. Folding and truncation of Unit B1 indicate  
379 another thrusting event. Unit C deposits on both sides of the folded Unit B1. Unit C1  
380 covers the folded Unit B1 and Unit C (Figure 9b). These features indicate that there is no  
381 more thrusting event rupturing the ground surface after the deposition of Units C and C1.

382 The basal age of Unit A is  $39.77 \pm 6.38$  ka. The middle Unit B1 has an age of  
383  $32.63 \pm 2.27$  ka. The boundary age between Unit B1 and Unit C is  $6.16 \pm 0.52$  ka (Xu et  
384 al. 2018a). Therefore, the thrusting event recorded by folding of Unit A is in the age  
385 bracket between  $39.77 \pm 6.38$  ka to and  $32.63 \pm 2.27$  ka. The event represented by folding  
386 of Unit B1 slightly postdates  $6.16 \pm 0.52$  ka. The displacement of Unit B and Unit B1  
387 indicates that the coseismic slip of the last event is  $1.70 \pm 0.15$  m at this site (Figure 9b).  
388 The error is resulted from identifying the boundary of sedimentary units, which is no  
389 more than 0.15 m.

390

### 5.1.2 Active folding

391

392

393

394

395

396

397

398

399

400

401

402

403

The active axial surface B' fixes to the tip of the SZG wedge structure and extends to the ground surface (Figures 5b and 8) or terminates below the SZG ramp (Figure 6b). With the southwest-vergent thrusting by the wedge structure, the active axial surface B' passes through and folds recent alluviums, and abandoned geomorphic markers. Along the most southwestern edge of YXL, the axial surface B' is located to the southwest of the SZG ramp (Figure 8). Therefore, the fold scarp corresponding to the axial surface B' is located to the southwest of the SZG ramp trace (Figures 8, 10a and 10b). The topographic profile crossing the southwestern edge of SZG-YSS has two inflection points (Figures 10a and 10b). One is at the outcrop of the SZG ramp, and another is at the trace of the axial surface B' (Figures 10a and 10b). The sub-horizontal topography in the northeast of the SZG indicates that the hanging wall uplifts as a rigid block; and the topographic slope between the ramp and the axial surface B' is  $\sim 9.9\%$  (or  $\sim 5.7^\circ$ ), which is significantly steeper than  $\sim 2.9\%$  (or  $\sim 1.7^\circ$ ) of the desert surface in the southwest of YXL (Figure 10b).

404

405

406

407

408

409

410

411

412

413

414

415

416

417

418

419

420

421

422

423

A trench exposes recent alluviums (Figures 11a and 11b). Among them, Upg1 through Upg4 maintain the constant thickness and the dip angle. Ug1 laps on Upg4 and pinches out at  $\sim 8.2$  m (Figure 11b). Ug2 laps on Ug1 to tapers out at  $\sim 4.7$  m (Figure 11b). Ug3 is an aeolian sediment layer with the constant thickness, covering Upg4, Ug1, and Ug2 in disconformity. Ug4, a constant thickness layer of alluviums, rests on Ug3. Upg1 through Ug2 have an identical angle, indicating that they widen by kink band migration. The width of the kink bands increases gradually with the thrusting of the SZG wedge structure (Figure 11c). Pinch-outs of Ug1 and Ug2 represent two thrusting events of the wedge structure in depth. Their total widths are not exposed, but their difference is  $3.5 \pm 0.15$  m, providing the coseismic displacement of the buried wedge structure during the thrusting event represented by the pinch-out of Ug1. The age of the lower-middle Ug1 is  $94.93 \pm 7.98$  ka, and the age of the middle Ug3 is  $59.43 \pm 3.42$  ka. They bracket the age of this thrusting event, but closer to  $94.93 \pm 7.98$  ka. The definite sedimentary record of the event is the boundary between Ug1 and Ug2. The sedimentation rate of Ug3 and Ug4 accelerates to cover folded Ug2. Folding of these sediments (Figure 11b) indicates that the trench does not cross the axial surface B', which may be approximately located at the dashed rectangular in Figure 11c. The top envelope dip angle of the growth strata (Figure 11c) is in response to the topographic slope between the SZG ramp trace and the axial surface B' (Figures 10a and 10b), which is smaller than the angle of the kink band over the lower SZG wedge structure (Figures 11a, 11b and 11c).

424

### 5.2 Active folding along the northeastern edge of YXL

425

426

427

428

429

430

431

432

433

The northeastern edge of YXL is an active fold scarp (Figures 12 and 13). In the northeast of the scarp, there exists an even playa covered by alluviums and diluviums. In the southwest of the scarp, there are rugged and inaccessible mountains of YXL. The northwesternmost part of YXL along the scarp is eroded to form a planation surface being ca. 30 m higher than the playa, marking the border of the low-angle northeastern limb of the XSQ-YQZ anticline (Figures 12, 13a and c). The seasonal stream-cut section (Figure 13a) shows that gravel layer T on the southwestern scarp tread descends northeastwards and splits from the topographic surface. Recent alluviums are folded and thin out toward the scarp (Figures 13a and c). Dips of the alluviums below the T level

434 become higher southwestwards to equal to the dip of the Qigequan Formation. At the  
435 scarp, the Qigequan Formation is covered by recent alluviums to form a growth  
436 unconformity (Figures 13a and c). Long topographic profiles crossing the scarp show the  
437 scarp height of ~30–31 m (Figures 13b and d).

## 438 6. Discussion

439 We present the coseismic slips, rupture area, seismic moment, moment  
440 magnitude, geometry, and historical deformation of the March 28, 2019 Mangya Mw  
441 5.04 earthquake fault. These new findings can improve our understanding of mechanisms  
442 of earthquakes and active tectonics in the northwestern Qaidam Basin, northern Tibet.

### 443 6.1 The relationship between the coseismic underground slip, the SZG ramp and 444 the March 28, 2019 Mangya earthquake

445 The measured underground rupture area and the slips along the SZG ramp suggest  
446 an earthquake of  $M_w 5.47 \pm 0.16$ . This result is comparable with  $M_w 5.04$ ,  $M_s 5.0$  (China  
447 Earthquake Data Center, 2019) and  $M_w 4.8 \pm 0.117$  (USGS, 2019) obtained from seismic  
448 wave inversion.

449 The mainshock and aftershocks measured by China Earthquake Data Center  
450 (2019) and USGS (2019) are not exactly in the extent derived from borehole  
451 deformations (Figure 2). However, the shock occurrence times are the same; therefore,  
452 they should record the same shocks. Moreover, the focus depths of the main shock of  $10$   
453  $\pm 1.8$  km (USGS, 2019),  $9 \pm 1.8$  km (China Earthquake Data Center, 2019) and  $\sim 9.5$  km  
454 have been reported, which are significantly distinct from the depths of the coseismic  
455 rupture ranging from  $\sim 1700$  m –  $\sim 2110$  m. Nevertheless, the depths of the coseismic  
456 rupture are identical with the SZG ramp (Figures 6a and 6b). The time of the borehole  
457 deformation is the same as the mainshock. The magnitude predicted by the true coseismic  
458 underground rupture area and slips approximates the measured magnitudes. One plane of  
459 the focal mechanism solution of the mainshock is identical to the results derived from  
460 borehole deformation and hydrocarbon seismic exploration. The SZG ramp is the only  
461 active fault evidenced by surface geology observations. Therefore, we conclude that the  
462 SZG ramp, the uppermost segment of the YXL thrust system, is the seismogenic fault of  
463 the March 28, 2019  $M_w 5.04$  Mangya earthquake, considering large uncertainties in  
464 measurements of the focus depths and epicenters.

### 465 6.2 Seismic potentials of the YXL thrust system

466 Seismic exploration reveals the geometry of the SZG ramp, the uppermost  
467 segment of the YXL thrust system. The surface deformation along both edges of YXL  
468 demonstrates that the entire YXL thrust system is active. Accordingly, we suggest that  
469 the earthquakes of the January 2, 1977  $M 6.4$  and  $M 5.1$ , as well as the February 26, 1987  
470  $M 6.1$  at the YXL area (Wang et al., 1999) were generated by thrusting of one part of the  
471 YXL thrust system. These thrusting events in recent decades did not rupture or fold  
472 ground surface and recent alluviums. This phenomenon suggests that the small-scale  
473 coseismic slips of these thrusting events are locked by an unruptured segment in front of  
474 the ruptured segments to accumulate more elastic strain in the hanging wall.

475 Alternatively, these slips may be completely absorbed by the growth of the YXL  
476 anticlinorium.

477 The surface ruptures and folded alluviums indicate that the coseismic slip per  
478 event can reach up to  $1.7 \pm 0.15$  m –  $3.5 \pm 0.15$  m, suggesting that the entire YXL thrust  
479 system probably ruptures. Seismic exploration shows that the YXL thrust system  
480 underlies the YXL anticlinorium. We can approximately use the surface extent of  $3200 \pm$   
481  $160$  km<sup>2</sup> of the anticlinorium as the area of the thrust system, ignoring the changes in its  
482 geometry. Using the equations (3) and (4), with the fault area of  $3200 \pm 160$  km<sup>2</sup>, the  
483 average coseismic slips of  $1.7 \pm 0.15$  m and  $3.5 \pm 0.15$  m over the thrust system as well as  
484 the shear modulus of  $30 \times 10^9$  N/m<sup>2</sup>,  $M_w$   $7.44 \pm 0.18$  and  $M_w$   $7.65 \pm 0.03$  can be  
485 obtained. This estimate means that the entire rupture of the YXL thrust system has the  
486 potential to generate  $M_w$   $7.65 \pm 0.03$  earthquakes. If each segment ruptures separately,  
487 the thrust system can produce earthquakes with magnitudes less than  $M_w \sim 7.6$ .

### 488 6.3 Growth mechanism the YXL anticlinorium

489 Surface deformation and seismic interpretation indicate that the southwest-  
490 directed thrusting to fold the hanging wall of the YXL thrust system to form the  
491 anticlinorium. The growth of the YXL anticlinorium creates the highest peak of  $\sim 3835$ m  
492 at the core of the GCG anticline, decreasing southeastwards to the average elevation of  
493  $\sim 3000$  m of the Qaidam Basin. This suggests that the displacements of the YXL thrust  
494 system wane southeastwards. Growth strata indicate that the SZG-YSS anticline has been  
495 initiated since the early Middle Miocene ( $\sim 16.5 - \sim 17.2$  Ma).

## 496 7 Conclusions

497 The SZG ramp, the uppermost part of the YXL thrust system, is the seismogenic  
498 fault of the March 28, 2019  $M_w$  5.04 Mangya earthquake. The partial SZG ramp ruptured  
499 during this event with a rupture area of  $45.30 \pm 10.24$  km<sup>2</sup>, a maximum slip of  $400 \pm 13$   
500 mm and the fault dip of  $\sim 38.6^\circ$ . These parameters generate a seismic moment of  $(1.81 \pm$   
501  $0.47) \times 10^{17}$  Nm and a moment magnitude of  $5.47 \pm 0.16$ . The long-term average slips of  
502 the thrust system range from  $\sim 0.2$  mm/yr to  $0.3$  mm/yr since the early Middle Miocene.  
503 The ramp of the thrust system ruptured the ground surface along the southwestern edge of  
504 YXL at  $\sim 35.91$  ka and  $6.16 \pm 0.52$  ka. The last thrusting event has a coseismic slip of  $1.7$   
505  $\pm 0.15$  m. The earlier coseismic folding events indicate that the coseismic displacement of  
506 the thrust system can reach up to  $3.5 \pm 0.15$  m. The YXL thrust system has the potential  
507 to generate  $M_w$   $7.65 \pm 0.03$  earthquakes. Growth strata indicate that YXL has been  
508 initiated since the early Middle Miocene ( $\sim 16.5 - \sim 17.2$  Ma).

## 509 Appendix A: The SZG-YSS anticline and its related fault

510 The  $\sim 60$ -km-long SZG-YSS anticline trends northwest and plunges toward the  
511 southeast at the Mangya Lake. The anticline is divided into the NW, middle and SE  
512 segments based on changes in trends of its axial trace (Figure 1). The axis of the NW  
513 segment strikes northwest. The SW limb of the NW segment dipping northeast is  
514 overturned at high angles (Figure 8), and is cut by the SZG ramp. The core of the NW  
515 segment is composed of the broad, sub-horizontal Shangyousha Shan Formation (Figure  
516 8). The NE limb of the NW segment consists of the Shangyousha Shan and the Shizigou

517 Formations dipping toward the northwest at  $\sim 25^\circ$ . The middle segment strikes north-  
518 south. The sub-vertical or somewhere overturned SW limb of this segment is made up of  
519 the Shangganchaigou Formation. The sub-horizontal Shangganchaigou Formation crops  
520 out in the core of this segment. The NE limb contains the Shangyousha Shan and  
521 Shizigou Formations dipping toward the northeast-east at  $\sim 15^\circ$ . The axis of the SE  
522 segment strikes northwest. The SW limb of this segment contains the sub-vertical or  
523 slightly overturned Xiayousha Shan, Shangyousha Shan, and Shizigou Formations. Its  
524 core consists of the horizontal Xiayousha Shan Formation. The NE limb of this segment  
525 includes the Xiayousha Shan, Shangyousha Shan and Shizigou Formations dipping to the  
526 northeast at  $\sim 10^\circ$ .

527 The profiles of [Figures 5a, 5b, 6a and 6b](#) cross southwestwards the Shizigou  
528 segment of the SZG-YSS anticline. We analyzed the fine changes in attitudes of seismic  
529 reflectors to locate a few regions of homogenous dip. There exist continuous reflectors  
530 covering the SZG-YSS anticline. At the crest of the anticline, there exist sub-horizontal  
531 reflectors between the axial surfaces C and C' from the ground surface to the SZG ramp.  
532 Below the growth axial surface G, the reflectors between the active axial surface A and  
533 the inactive axial surface A' dip to the northeast at  $\sim 13^\circ$ . Northeast of the axial surface C  
534 and above the growth axial surface G, there are sub-horizontal reflectors. Below the SZG  
535 ramp, northeast of the axial surface B' and above the SZG back ramp, there exist curved  
536 reflectors with dips ranging from  $\sim 15^\circ$  to  $\sim 26^\circ$ . Above the SZG flat, below the SZG back-  
537 ramp and southwest of the axial surface B, there exist reflectors dipping to the southwest  
538 at  $\sim 23^\circ$ ; there are horizontal reflectors between the axial surfaces B and A', and below the  
539 SZG back-ramp; there exist reflectors dipping to the northeast at  $\sim 13^\circ$  between the axial  
540 surfaces A and A', and below the growth axial surface G. These three regions of  
541 homogeneous dip constitute the lower SZG wedge structure, a buried fault-bend fold  
542 anticline ([Figures 5b and 6b](#)). There are the horizontal regions of homogeneous dip  
543 between the axial surfaces A and D' and above the GCG flat, constituting the syncline  
544 between the SZG-YSS and the GCG anticlines. Below the SZG flat, the lower SZG ramp,  
545 and the GCG flat are regional low-angle reflectors ([Figures 5b and 6b](#)).

546 We put forward the structural interpretation of the southwestern SZG-YSS  
547 anticline ([Figures 5b and 6b](#)) based on above-mentioned locating of regions of  
548 homogeneous dip. The well-imaged fault reflectors define the northeast-dipping SZG  
549 ramp, separating the arcuate reflectors below it from the noisy region representing the  
550 high angled overturned SW limb of the NW SZG-YSS anticline above it ([Figures 5a, 5b,](#)  
551 [6a and 6b](#)). Reflectors above and below the SZG back-ramp are disharmonious, which  
552 evidences the fault; the SZG back-ramp terminates upward at the lower end of the axial  
553 surface C' to connect with the SZG ramp. The axial surface B' terminates downward at  
554 the SZG wedge tip and upward below the SZG back-ramp. The SZG flat occurs between  
555 lower ends of the axial surface B and B'. The connection of the downward terminations  
556 of the axial surfaces A and A' is interpreted as the lower SZG ramp. The connection of  
557 the downward terminations of axial surfaces A and D' is interpreted as the GCG flat. This  
558 structural interpretation ([Figures 5b and 6b](#)) predicts that the southwest-vergent thrusting  
559 by the YXL thrust system produces the lower SZG anticline (the SZG wedge structure),  
560 the northwestern SZG-YSS anticline and surface deformations.

561 The SE SZG-YSS anticline strikes southeast (Figure 1). Its SW limb dips to the  
562 southwest at  $\sim 50^{\circ}$ – $80^{\circ}$  decreasing southeastward, but overturns somewhere, and is cut by  
563 a thrust (Xu et al., 2018b). The seismic profile (Figure 7b) images the limb poorly. Its  
564 crest consists of sub-horizontal reflectors, agreeing with surface geology observations.  
565 The region of homogeneous dip between the axial surfaces A and A' defines the NE limb  
566 dipping to the northeast at  $\sim 21^{\circ}$ , in agreement with surface geology observations. The  
567 width of this region of homogeneous dip maintains constant in the pregrowth strata. This  
568 region narrows upward along the growth axial surface G. The axial surface A' splits  
569 upward into the growth axial surface G and G1. The crest of the anticline is the region of  
570 homogeneous dip between the axial surfaces B and A', merging downwards to form the  
571 axial surface AB extending downward to the SZG ramp. We suppose the structural  
572 interpretation that the SE SZG-YSS anticline is a forelimb breakthrough fault-  
573 propagation fold anticline (Figure 7b) according to locating of regions of homogeneous  
574 dip and the growth fault-propagation folding theory (Suppe and Medwedeff, 1990; Suppe  
575 et al., 1992).

#### 576 **Appendix B: The GCG anticline and its related fault**

577 The GCG anticline is in the middle of the YXL anticlinorium, plunging to the  
578 southeast (Figure 1). The SW limb of the anticline dips to the southwest at  $\sim 35^{\circ}$ , and the  
579 NE limb dips northeast at  $\sim 25^{\circ}$  (Figure 5b). Dip angles of both limbs lower toward the  
580 southeast. The horizontal region of homogeneous dip between the axial surfaces A and D'  
581 corresponds to the syncline between the SZG-YSS and the GCG anticlines (Figures 5a  
582 and 5b). The SW limb of the anticline is made up of the  $\sim 28^{\circ}$ -southwest-dipping and  
583  $\sim 4.9$ -km-long region of homogeneous dip. This region extends upward to the ground  
584 surface and downward to the GCG flat. The horizontal region of homogeneous dip  
585 terminating downward at the GCG flat between D and E' consists of the crest of the  
586 anticline. The region of homogeneous dip between the axial surfaces E and E' dips to the  
587 northeast at  $\sim 11^{\circ}$  and have a width of  $\sim 5.4$  km, consisting of the NE limb. The region  
588 extends upward to the ground surface and downward to the GCG ramp. The horizontal  
589 region of homogeneous dip between the axial surface E and F' is composed of a syncline  
590 between the GCG and the XSQ-YQZ anticlines. On basis of above-mentioned locating  
591 regions of homogeneous dip, we interpret GCG as a classic fault-bend fold anticline  
592 (Figure 5b).

#### 593 **Appendix C: The XSQ-YQZ anticline and its related fault**

594 The XSQ-YQZ anticline is the northeastern part of the YXL anticlinorium (Figure  
595 1). Its middle segment plunges (Figure 1). The SW limb dips to the southwest at a high  
596 angle; the NE limb dips to the northeast at a lower angle, but changes significantly.  
597 Figure 5b shows that the anticline consists of four regions of homogeneous dip. The  
598 horizontal region of homogeneous dip between the axial surfaces E and F' represents the  
599 syncline between the XSQ-YQZ and the GCG anticlines, narrowing upward and  
600 widening downward until the GCG flat. The axial surface F' serves as the synclinal axial  
601 one of the SW limb. The region of homogeneous dip between the axial surfaces F and F'  
602 maintains a constant width and dips to the southwest at  $\sim 20^{\circ}$  to form the SW limb of the  
603 anticline. The region of the homogeneous dip between the axial surfaces F and H' dips to  
604 the northeast at  $\sim 7.5^{\circ}$  and widens upward from the upper XSQ ramp to form the crest of



605 the anticline. The region of homogeneous dip between the axial surfaces F and H' dips  
606 northeast at  $\sim 20^\circ$ . The seismic profile 4 km northwest of Figure 5a shows that this region  
607 turns into being horizontal. So, we deduce the existence of the axial surface H, and that  
608 the width between the axial surfaces H and H' is the minimum. There exist sub-horizontal  
609 reflectors below this region of homogeneous dip, which form a disharmony. According to  
610 locating regions of homogeneous dip in the seismic profile (Figures 5a and 5b), we  
611 interpret the XSQ-YQZ as a multi-fault bend fold anticline.

## 612 **Appendix D: The Shaxi wedge structure**

613 The buried Shaxi structure is revealed by seismic exploration. It is well imaged as  
614 a monocline consisting of a kink band between the axial surface M, M' and Gs, and the  
615 horizontal regions of homogeneous dip in its both sides (Figures 5b and 6b). The kind  
616 band between the axial surface Gs and M, above the middle member of the  
617 Xiaganchaigou Formation, narrows upward and fades away in the middle part of the  
618 Shangyousha Shan Formation. It maintains a constant width between the axial surfaces M  
619 and M' and extends to  $\sim 3.5$  s in time-depth. Based on locating regions of homogeneous  
620 dip (Figure 5b and 6b), we interpret Shaxi as a wedge structure.

## 621 **Acknowledgment**

622 This study benefited from discussions with Profs. Zhaojie Guo, Zhouchuan  
623 Huang, and Tao Wang. This study was supported by the National Natural Science  
624 Foundation of China (grants 41672198 and 41372201), the National Key R&D Plan  
625 (Grant No. 2017YFC0601402), and the Major National R&D Projects Programs of China  
626 (2016ZX05003-006). LABEX VOLTAIRE (ANR-10-LABX-100-01), and EQUIPEX  
627 PLANET (ANR-11-EQPX-0036) are appreciated. The focus parameters of the March 28,  
628 2019 Mw 5.04 Mangya earthquake and aftershocks from China Earthquake Data Center  
629 website presented in this manuscript can be found online via Mendley  
630 (<https://www.mendeley.com/>) at <http://dx.doi.org/10.17632/npbw484bgf.1>.

## 631 **References**

- 632 Bian, Q., Zhang, D., Yu, X., Cheng, X., Du, W., Liu, R., Wang, Z. and Guo, Z., 2019,  
633 Transpressional salt tectonic system in western Qaidam Basin, Western China, AAPG  
634 Bulletin, v. 103, no. 3, 547–568, doi:10.1306/08161817119.
- 635 Chang, H., Li, L., Qiang, X., Garzzone, C. N., Pullen, A., An, Z., 2015,  
636 Magnetostratigraphy of Cenozoic deposits in the western Qaidam Basin and its  
637 implication for the surface uplift of the northeastern margin of the Tibetan Plateau, Earth  
638 and Planetary Science Letters, 430, 271–283,  
639 <http://dx.doi.org/10.1016/j.epsl.2015.08.029>
- 640 Cheng, X., D. Zhang, M. Jolivet, X. Yu, W. Du, R. Liu, and Z. Guo, 2018, Cenozoic  
641 structural inversion from transtension to transpression in Yingxiong Range, western  
642 Qaidam Basin: New insights into strike-slip superimposition controlled by Altyn Tagh  
643 and Eastern Kunlun Faults: Tectonophysics, v. 723, p. 229–241,  
644 doi:10.1016/j.tecto.2017.12.019.

645 Chen Y., V. Courtillot, J.P. Cogné, J. Besse, Z. Yang and R. Enkin, 1993, The  
646 configuration of Asia prior to the collision of India: Cretaceous paleomagnetic  
647 constraints, *Journal of Geophysical Research*, 98, 21, 927 – 21,941.

648 Chen Y., S. Gilder, N. Halim, J.-P. Cogné, and V. Courtillot, 2002, New Mesozoic and  
649 Cenozoic data help constrain the age of motion on the Altyn Tagh fault and rotation of  
650 the Qaidam basin, *Tectonics*, doi: 10.1029/2001TC901030.

651 Cheng, F., Garzzone, C. N., Jolivet, M., Guo, Z., Zhang, D., Zhang, C., & Zhang, Q.  
652 (2019). Initial deformation of the northern Tibetan Plateau: Insights from deposition of  
653 the Lulehe Formation in the Qaidam Basin. *Tectonics*, 38.  
654 <https://doi.org/10.1029/2018TC005214>.

655 Chen, X.H., Dang, Y.Q., Yin, A., et al., 2010, *The Basin-mountain Coupling and*  
656 *Evolution of Qaidam Basin and Its Surrounding Mountains*, Beijing: Geological  
657 Publishing House, 1-437. (in Chinese).

658 China Earthquake Data Center, 2019, <http://data.earthquake.cn>

659 Feng, G., Hetland, E. A., Ding, X., Li, Z., Zhang, L., 2010, Coseismic fault slip of the  
660 2008 Mw 7.9 Wenchuan earthquake estimated from InSAR and GPS measurements,  
661 *Geophysical Research Letters*, v. 37, L01302, doi:10.1029/2009GL041213.

662 Huang, H., Huang, Q., and Ma, Y., 1996, *Geology of Qaidam Basin and its petroleum*  
663 *prediction*: Beijing, Geological Publishing House, 257 p.

664 Horton, B.K., 2012, *Cenozoic evolution of hinterland basins in the Andes and Tibet*, IN:  
665 Busby and A. Azor, 2012, *Tectonics of sedimentary basins: Recent Advances*, John  
666 Wiley & Sons, Ltd, West Sussex, PO19 8SQ, UK.

667 Huo, G.M., ed., 1990, *Petroleum geology of China: Oil fields in Qinghai and Xizang*:  
668 Chinese Petroleum Industry Press, v. 14, 483 p.

669 Hubert-Ferrari, A., Suppe, J., Gonzalez-Mieres, R. and Wang, X., 2007, Mechanisms of  
670 active folding of the landscape (southern Tian Shan, China), *Journal of Geophysical*  
671 *Research*, v. 112, B03S09, doi: 10.1029/2006JB004362

672 Huang, K., Chen, L., Xiao, A., Shen, Y., Cenozoic Deformation Characteristics of the  
673 Xianshuiquan Anticline in the Northwestern Qaidam Basin and Its Significance,  
674 *Geological Journal of China Universities*, V. 24, No.5, 761-768. (In Chinese with  
675 English abstract)

676 Liu-Zeng, J., Zhang, Z., Wen, L., Tapponnier, P., Sun, J., Xing, X., Hu, G., Xu, Q., Zeng,  
677 L., Ding, L., Ji, C., Hudnut, K.W., van der Woerd, J., Co-seismic ruptures of the 12 May  
678 2008, Ms 8.0 Wenchuan earthquake, Sichuan: East–west crustal shortening on oblique,  
679 parallel thrusts along the eastern edge of Tibet, *Earth and Planetary Science Letters*, v.  
680 286 , 355–370, doi:10.1016/j.epsl.2009.07.017.

681 Molnar, P. and Tapponnier, P., 1975, Cenozoic tectonics of Asia: Effects of continental  
682 collision, *Science*, 189,419-426.

683 Mueller, K., Suppe, J., 1997, Growth of Wheeler Ridge anticline, California: geomorphic  
684 evidence for fault-bend folding behaviour during earthquakes, *Journal of Structural*  
685 *Geology*, v. 19, issues 3-4, 383-396, [https://doi.org/10.1016/S0191-8141\(96\)00112-5](https://doi.org/10.1016/S0191-8141(96)00112-5)

- 686 Medwedeff, D. A., 1989, Growth fault-bend folding at southeast Lost Hills, San Joaquin  
687 Valley, California: AAPG Bulletin, v. 73, p. 54–67.
- 688 Medwedeff, D. A. and J. Suppe, 1997, Multibend fault-bend folding: Journal of  
689 Structural Geology, 19, p. 279–292.
- 690 Pang, J., Yu, J., Zheng, D., Wang, W., Ma, Y., Wang, Y., et al. 2019. Neogene expansion  
691 of the Qilian Shan, north Tibet: Implications for the dynamic evolution of the Tibetan  
692 Plateau. *Tectonics*, 38, 1018–1032. <https://doi.org/10.1029/2018TC005258>
- 693 Pan JW, Li HB, Sun ZM, Liu DL, Wu C and Yu CQ. 2015. Tectonic responses in the  
694 Qaidam basin induced by Cenozoic activities of the Altyn Tagh fault. *Acta Petrologica  
695 Sinica*, 31(12): 3701-3712 (in Chinese with English abstract)
- 696 Qinghai BGMR (Qinghai Bureau of Geology and Mineral Resources), 1991, Regional  
697 geology of Qinghai Province: Beijing, Geological Publishing House.
- 698 Qiu, N., 2002, Tectono-thermal evolution of the Qaidam Basin, China: Evidence from Rb  
699 and apatite fission track data: *Petroleum Geoscience*, v. 8, p. 279–285.
- 700 Rieser, A.B., Liu, Y.J., Genser, J., Neubauer, F., Handler, R., Friedl, G., and Ge, X.H.,  
701 2006a, 40Ar/39Ar ages of detrital white mica constrain the Cenozoic development of the  
702 intracontinental Qaidam Basin: *Geological Society of America Bulletin*, v. 118, p. 1522–  
703 1534, doi: 10.1130/B25962.1.
- 704 Rieser, A.B., Liu, Y.J., Genser, J., Neubauer, F., Handler, R., and Ge, X.H., 2006b,  
705 Uniform Permian 40Ar/39Ar detrital mica ages in the eastern Qaidam Basin (NW China):  
706 Where is the source?: *Terra Nova*, v. 18, p. 79–87, doi: 10.1111/j.1365-  
707 3121.2005.00666.x.
- 708 Song, T., and Wang, X., 1993, Structural styles and stratigraphic patterns of  
709 syndepositional faults in a contractional setting: Examples from Qaidam basin,  
710 northwestern China: AAPG Bulletin, v. 77, p. 102–117.
- 711 Sun, Z.M., Yang, Z.Y., Pei, J.L., Ge, X.H., Wang, X.S., Yang, T.S., Li, W.M., and Yuan,  
712 S.H., 2005, Magnetostratigraphy of Paleogene sediments from northern Qaidam basin,  
713 China: Implications for tectonic uplift and block rotation in northern Tibetan plateau:  
714 *Earth and Planetary Science Letters*, v. 237, p. 635–646, doi: 10.1016/j.epsl.2005.07.007.
- 715 Suppe, J., 1983, Geometry and Kinematics of fault-bend folding, *American Journal of  
716 Science*, 283, 684-721.
- 717 Suppe, J. and Medwedeff, 1990, Geometry and Kinematics of fault-propagation folding,  
718 *Eclogae Geologicae Helveticae*, 83
- 719 Suppe, J.S., Chou, G.T., and Hook, S.C. (1992) Rates of folding and faulting determined  
720 from growth strata. In McClay, K.R. (ed.), *Thrust Tectonics*, pp. 105–122. Chapman and  
721 Hall, London.
- 722 Suppe, J., Sabat, F., Muñoz, J.A., Poblet, J., Roca, E., and Vergés, J. (1997) Bed-by-bed  
723 fold growth by kink-band migration: Sant Llorenç de Morunys, Eastern Pyrenees. *Journal  
724 of Structural Geology*, 19, 443–461.

725 Tapponnier, P. and Molnar P., 1976, Slip-line field theory and large-scale continental  
726 tectonics, *Nature*, 264 (5584): 319~ 324.

727 Tapponnier, P. and Molnar, P., 1977, Active faulting and tectonics in China, *Journal of*  
728 *Geophysics Research*, 82(20), 2905–2930, doi: 10.1029/JB082i020p02905.

729 Tapponnier, P. and Molnar, P., 1979, Active faulting and Cenozoic tectonics of the Tien  
730 Shan, Mongolia, and Baykal regions, *Journal of Geophysical Research*, v. 84, no. B7,  
731 3425-3459.

732 Tapponnier, P, Peltzer, G., Le Dain, A. Y., Armijo, R., Cobbold P., 1982, Propagating  
733 extrusion tectonics in Asia: New insight s from simple experiments with plasticine,  
734 *Geology*, 10: 611 ~ 616.

735 Tapponnier, P, Xu, Z.Q., Roger, F., Meyer, B., Arnaud, N., Wittlinger, G., Yang, J.S.,  
736 2001, Oblique stepwise rise and growth of the Tibet plateau, *Science*, 294, 1671-1677,  
737 DOI: 10.1126/science.105978

738 USGS (U.S. Geological Survey), 2019,  
739 <https://earthquake.usgs.gov/earthquakes/eventpage/us2000k66p/executive>

740 Wang, S., Wu, G., Shi, Z., 1999, *Catalogue of Chinese Earthquakes (1912–1990, MS*  
741 *≥4.7)*, Beijing: China Science and Technology Press.

742 Wang, C., Dai, J., Zhao, X., Li, Y., Grahamd, S. A., He, D., Ran, B., Meng, J., 2014,  
743 *Outward-growth of the Tibetan Plateau during the Cenozoic: A review*, *Tectonophysics*,  
744 621, 1–43, <http://dx.doi.org/10.1016/j.tecto.2014.01.036>.

745 Wang, W., Qiao, X., Yang, S., Wang, D., 2017a, Present-day velocity field and block  
746 kinematics of Tibetan Plateau from GPS measurements, *Geophysical Journal*  
747 *International*, 208, 1088–1102, doi: 10.1093/gji/ggw445.

748 Wang, W., Zheng, W., Zhang, P., Li, Q., Kirby, E., Yuan, D., Zheng, D., Liu, C., Wang,  
749 Z., Zhang, H. & Pang, J., 2017b, Expansion of the Tibetan Plateau during the Neogene.  
750 *Nat. Commun.* 8, 15887 doi: 10.1038/ncomms15887.

751 Wells, D. L., and K. J. Coppersmith, 1994, New empirical relationships among  
752 magnitude, rupture length, rupture width, rupture area, and surface displacement, *Bull.*  
753 *Seismol. Soc. Am.*, 84, 974-1002.

754 Wu C., Yan C.F., Li H.B., Tian G.R., Sun Z.M., Liu D.L., Yu C.Q. and Pan J.W., 2013,  
755 *Cenozoic tectonic evolution of the western Qaidam Basin and its constrain on the growth*  
756 *of the northern Tibetan Plateau. Acta Petrologica Sinica*, 29(6): 2211–2222

757 Wu, W., Yuan, J., Wang, J., Shi, Y., Chen, Y., Zou, K., Jia, D., 2020, A Late Neogene  
758 framework and transpressional system within the Yingxiongling Range, western Qaidam  
759 Basin, Northeast Tibetan Plateau: Insights from seismic reflection profiles and active  
760 tectonics, *Journal of Asian Earth Sciences*, DOI:  
761 <https://doi.org/10.1016/j.jseaes.2019.104061>

762 Xia, W., Zhang, N., Yuan, X., Fan, L., and Zhang, B., 2001, Cenozoic Qaidam basin,  
763 China: A stronger tectonic inversed, extensional rifted basin: *AAPG Bulletin*, v. 85, p.  
764 715–736.

765 Xu, C., Liu, Y., Wen, Y., Wen, Y., Wang, R.-Q., 2010, Coseismic Slip Distribution of the  
766 2008 Mw 7.9 Wenchuan Earthquake from Joint Inversion of GPS and InSAR Data,  
767 Bulletin of the Seismological Society of America, 100(5B): 2736-2749, DOI:  
768 10.1785/0120090253.

769 Xu, J., Hui, X., Cheng, H., Zhang, X., Shang, S., 2108a, Analysis on Late Quaternary  
770 Tectonic Deformation of the Shizigou Fault, Southwestern Margin of the Qaidam Basin,  
771 Journal of Seismological Research, v.41, no.1, 46-54. (In Chinese with English abstract)

772 Xu, J., Hui, X., Cheng, H., Zhang, X., Shang, S., 2108b, Paleoseismology and late  
773 Quaternary slip rate of the Youshashan fault at southern margin of Qaidam basin,  
774 Seismology and Geology, v.40, no.2, 465-479, doi: 10.3969 /j.issn.0253-  
775 4967.2018.02.013. (In Chinese with English abstract)

776 Xu, X., Wen, X., Yu, G., Chen, G., Klinger, Y., Hubbard, J., and Shaw, J., 2009,  
777 Coseismic reverse- and oblique-slip surface faulting generated by the 2008 Mw 7.9  
778 Wenchuan earthquake, China, Geology, 37 (6): 515–518,  
779 <https://doi.org/10.1130/G25462A.1>.

780 Yang, F., Ma, Z., Xu, T., and Ye, S., 1992, A Tertiary paleomagnetic stratigraphic profile  
781 in Qaidam basin: Acta Petrologica Sinica, v. 13, p. 97–101.

782 Yin, A. & Harrison, T.M. (2000) Geologic evolution of the Himalayan Tibetan Orogen.  
783 Annu. Rev. Earth Planet. Sci. 28, 211–80.

784 Yin, A., P. Rumelhart, R. Butler, E. Cowgill, T. Harrison, D. Foster, R. Ingersoll, Q.  
785 Zhang, X.-Q. Zhang, and X.-F. Wang, 2002, Tectonic history of the Altyn Tagh fault  
786 system in northern Tibet inferred from Cenozoic sedimentation: Geological Society of  
787 America Bulletin, v. 114, no. 10, p. 1257–1295, doi:10.1130/0016-  
788 7606(2002)114<1257:THOTAT>2.0.CO;2.

789 Yin, A., Dang, Y., Zhang, M., McRivette, M.W., Burgess, W.P., and Chen, X., 2007,  
790 Cenozoic tectonic evolution of Qaidam basin and its surrounding regions (part 2): Wedge  
791 tectonics in southern Qaidam basin and the Eastern Kunlun Range, in Sears, J.W., Harms,  
792 T.A., and Evenchick, C.A., eds., Whence the Mountains? Inquiries into the Evolution of  
793 Orogenic Systems: A Volume in Honor of Raymond A. Price: Geological Society of  
794 America Special Paper 433, p. 369–390, doi: 10.1130/2007.2433(18).

795 Yin, A., Dang, Y.-Q., Wang, L.-C., Jiang, W.-M., Zhou, S.-P., Chen, X.-H., Gehrels,  
796 G.E., and McRivette, M.W., 2008a, Cenozoic tectonic evolution of Qaidam Basin and its  
797 surrounding regions (part 1): The southern Qilian Shan–Nan Shan thrust belt and  
798 northern Qaidam Basin: Geological Society of America Bulletin, v. 120, no. 7–8, p. 813–  
799 846, <https://doi.org/10.1130/B26180.1>.

800 Yin, A., Dang, Y.Q., Zhang, M., Chen, X.H., and McRivette, M.W., 2008b, Cenozoic  
801 tectonic evolution of the Qaidam Basin and its surrounding regions (Part 3): Structural  
802 geology, sedimentation, and regional tectonic reconstruction: Geological Society of  
803 America Bulletin, v. 120, no. 7–8, p. 847–876, <https://doi.org/10.1130/B26232.1>.

804 Yu, F., Y. Wang, X. Li, X. Li, and Z. Feng, 2011, Deformation characteristics and  
805 genesis simulation of the Shizigou-Youshashan structural belt in Qaidamu Basin:  
806 Geotectonica et Metallogenia, v. 2, p. 6.

807 Zhou, J., F. Xu, T. Wang, A. Cao, and C. Yin, 2006, Cenozoic deformation history of the  
808 Qaidam Basin, NW China: Results from cross-section restoration and implications for  
809 Qinghai–Tibet Plateau tectonics: *Earth and Planetary Science Letters*, v. 243, no. 1–2, p.  
810 195–210, doi: 10.1016/j.epsl.2005.11.033.

811 Zuza, A.V., Wu, C., Wang, Z., Levy, D. A., Li, B., Xiong, X., and Chen, X., 2019,  
812 Underthrusting and duplexing beneath the northern Tibetan Plateau and the evolution of  
813 the Himalayan-Tibetan orogen, *LITHOSPHERE*; v. 11; no. 2; p. 209–231,  
814 <https://doi.org/10.1130/L1042.1>

815 **Table 1.** Cenozoic stratigraphy of the YXL region, southwestern Qaidam Basin.  
 816 Simplified from [Bian et al. \(2019\)](#).

Formation	Age (Ma)	Symbol	Lithology
<b>Qigequan</b>	2.5	Q <sub>1q</sub>	Gray, grayish yellow conglomerate, pebbled sandstone, gray, grayish white sandy mudstone.
<b>Shizigou</b>	8.1	N <sub>2</sub> <sup>3s</sup>	Upper member: grayish white, brown mudstone, and interlayered siltstone. Lower member: pebbled sandstone, siltstone, argillaceous siltstone, and mudstone.
<b>Shangyousha Shan</b>	15.3	N <sub>2</sub> <sup>2sy</sup>	Gray, dark gray mudstone intercalated with dark gray calcareous mudstone.
<b>Xiayousha Shan</b>	20	N <sub>2</sub> <sup>1xy</sup>	Upper member: thick gray mudstone intercalated with marlstone and limestone. Lower member: gray mudstone intercalated with thin marlstone and siltstone.
<b>Shangganचाigou</b>	35.5	N <sub>1sg</sub>	Gray mudstone intercalated with siltstone.
<b>Upper Xianganचाigou</b>	37.8	E <sub>3</sub> <sup>2xg</sup>	Evaporate, gray mudstone, and calcareous mudstone intercalated with argillaceous siltstone.
<b>Lower Xianganचाigou</b>	43.8	E <sub>3</sub> <sup>1xg</sup>	Brown mudstone and interlayered fine-grained sandstone.
<b>Lulehe</b>		E <sub>1-2l</sub>	Upper member: mudstone interlayered with siltstone. Lower member: conglomerate.

817

818 **Table 2.** Logging of boreholes H6-2-510 from the depth of 1970 m to 1990 m, and H4-2-  
 819 506 from the depth of 1920 m to 2014 m.

Borehole name	Starting depth (m)	Ending depth (mm)	Thickness (m)	Normal inner diameter (mm)	Maximum inner diameter (mm)	Minimum inner diameter (mm)	Maximum radius (mm)	Minimum radius (mm)	Deformation amount (mm)
<b>H6-2-510</b>	1970.0	1990.0	20	247.91	254.86	172.88	128.12	47.60	75.03
<b>H4-2-506</b>	1920.0	1923.0	3.0	247.91	255.08	199.51	129.21	79.54	48.40
	1991.0	1997.0	6.0	247.91	259.19	245.75	131.64	119.61	2.16
	1997.0	2014.0	17.0	247.91	255.36	217.96	128.75	104.75	29.95

820

821 **Table 3.** Coseismic slips of the Mangya earthquake fault at the eight borehole sites.

<b>Borehole name</b>	<b>Latitude</b>	<b>Longitude</b>	<b>Depth of damage (m)</b>	<b>Offset (mm)</b>
<b>H4-3-414</b>	38°18'09"	90°55'25"	~2034.8	400 ± 13
<b>H4-3-510</b>	38°18'18"	90°55'28"	~2110.5	400 ± 13
<b>H4</b>	38°18'01"	90°55'18"	~1700.0	107 ± 42
<b>H6-2-510</b>	38°18'50"	90°55'06"	~1994.7	182 ± 58
<b>H4-2-506</b>	38°18'57"	90°54'50"	~1925.0	28 ± 21
<b>H2-3-413</b>	38°16'24"	90°54'49"	~1500.0	188 ± 59
<b>H4-3-411</b>	38°16'58"	90°54'21"	~2159.0	188 ± 59
<b>H4-2-510</b>	38°17'36"	90°54'05"	~2271.0	107 ± 42

822

823 **Table 4.** The focal mechanism solution of the March 28, 2019 Mw 5.04 Mangya  
824 Earthquake.

<b>Solution</b>	<b>Strike (°)</b>	<b>Dip (°)</b>	<b>Slip angle (°)</b>
<b>Plane 1</b>	302.4	20.2	134.0
<b>Plane 2</b>	76.5	75.6	75.7

825



826 **Figure 1.** (a) Simplified geological map of Yingxiong Ling (YXL), southwestern  
827 Qaidam. Lower-hemisphere focal mechanisms of the March 28, 2019 Mw 5.04 Mangya  
828 earthquake shows compressional quadrants in blue and dilational quadrants in clear.  
829 Locations of seismic profiles, [Figures 2, 8, and 12](#) are marked. (b) Shaded relief map  
830 showing major faults and topographic features of the Himalayan-Tibetan orogen. The  
831 black rectangular marks the location of [Figure 1a](#). Fault traces are from [Yin & Harrison](#)  
832 [\(2000\)](#) and [Tapponnier et al. \(2001\)](#). WS, Western Himalayan Syntaxis; ES, Eastern  
833 Himalayan Syntaxis; MMT, Main Mantle Thrust; AKMS, Ayimaqing–Kunlun–Mutztagh  
834 suture; JS, Jinsha suture; BNS, Bangonghu–Nujiang suture; IZS, Indus–Zangbo suture.

835 **Figure 2.** Coseismic slip contour map of the Shizigou (SZG) ramp on the March 28, 2019  
836 Mw 5.04 Mangya earthquake in Yingxiong Ling. Eight damaged boreholes define the  
837 coseismic underground rupture area of the event. Epicenters of the mainshock and  
838 aftershocks (See Table S1) are from [China Earthquake Data Center \(2019\)](#).

839 **Figure 3.** The offset drilling rod of borehole H4-3-414 showing that the low-angle SZG  
840 ramp cut it just at the faulting moment, and its possible fracturing process. See [Figure 2](#)  
841 for the borehole location. [Photo \(a\)](#) was shot when the pipe was pulled out from the hole,  
842 and [photo \(b\)](#) was shot when the pipe was laid down. The outer diameter of the drill pipe  
843 is 101.6 mm. (c) Configuration of the borehole structure before being offset. (d) The  
844 casing pipe is sheared, as the right side of the upper casing pipe just touches the right side  
845 of the drilling rod. (e) With the offset increasing, the left side of the lower casing pipe just  
846 touches the left side of the drilling rod. (f) The drilling rod near the fault plane is  
847 flattened. (g) The flattened drilling rod is bend like a kink and pulled cut. Assuming that  
848 the kink-like deformation of the drilling pipe rod is symmetrical relative to the broken  
849 surface and the pipe is just broken away, the offset is  $400 \pm 13$  mm.

850 **Figure 4.** Photos of the lead seal before being put into (a and b) and after being pulled out  
851 (c and d) from borehole H4-3-414. The diameter of the lead seal bottom is 165 mm and  
852 the inner diameter of the casing pipe is 166.63 mm. The side face of the lead seal has  
853 scratches, but no imprint exists in its bottom surface, revealing that the coseismic slip at  
854 this borehole site is more than 196.85 mm, the outer diameter of the casing pipe.

855 **Figure 5.** Clear (a) and interpreted seismic profiles (b) crossing the middle segment of  
856 the YXL anticlinorium. The rightmost segment separated from the main part is located to  
857 about 4 km northwest of the main part. See [Figure 1](#) for the location. LSZGA, the lower  
858 Shizigou anticline; SZGR, the Shizigou ramp; SZGBR, the Shizigou back-ramp; SZGF,  
859 the Shizigou flat; LSZGR, the lower Shizigou ramp; GCGF, the Ganchaigou flat; GCGR,  
860 the Ganchaigou ramp; XSQF, the Xianshuiquan flat; UXSQR, the upper Xianshuiquan  
861 ramp; LXSQR, the lower Xianshuiquan ramp; LXSQF, the lower Xianshuiquan Flat.

862 **Figure 6.** Clear (a) and interpreted seismic profiles (b) crossing the northwestern SZG-  
863 YSS anticline. See [Figures 1 and 2](#) for the location. The green line denotes the coseismic  
864 rupture segment of the SZG ramp on the March 28, 2019 Mw 5.04 Mangya earthquake.  
865 The vertical scale is equal to the horizontal one. LSZGA, the lower Shizigou anticline;  
866 SZGR, the Shizigou ramp; SZGBR, the Shizigou back-ramp; SZGF, the Shizigou flat;

867 LSZGR, the lower Shizigou ramp; GCGF, the Ganchaigou flat. Symbols are the same as  
868 in [Figures 5](#)

869 **Figure 7.** Clear (a) and interpreted seismic profiles (b) crossing the southeastern SZG-  
870 YSS anticline. The vertical scale is equal to the horizontal one. See [Figure 1](#) for the  
871 location. Symbols are the same as in [Figures 5](#) and [6](#). YSSR, the Youshan Shan ramp.

872 **Figure 8.** The folded topographic surface and a fault scarp along the southwestern edge  
873 of northwestern YXL. The red solid line with bars toward the upper plate marks the SZG  
874 ramp trace; the red dashed line marks the trace of the active axial surface B'. See the  
875 location in [Figure 1](#). The satellite image is sourced from Google Earth.

876 **Figure 9.** An outcrop photo of deformed alluviums by the SZG ramp (a) and its  
877 interpretation (b). Folding of Unit A and Unit B1 represents two thrusting events  
878 rupturing the ground surface. The event A happened between  $39.77 \pm 6.38$  ka and  $32.63 \pm$   
879  $2.27$  ka, and event B1 at  $6.16 \pm 0.52$  ka (ages after [Xu et al., 2018a](#)). See the location in  
880 [Figure 8](#).

881 **Figure 10.** The folded topographic surface and the fault scarp along the southwestern  
882 edge of northwestern YXL. (a) A photo of the fold and the fault scarps. (b) A topographic  
883 profile crossing the southwestern edge of YXL. The right side of the photo points to the  
884 northwestern SZG-YSS anticline. The two topographic inflection points correspond to the  
885 outcrop of the SZG ramp and the axial surface of B', respectively. See the location in  
886 [Figure 8](#).

887 **Figure 11.** (a) A trench photo of the folded sediments produced by southwest-vergent  
888 thrusting of the lower SZG wedge structure. See location in [Figure 8](#). (b) Reinterpretation  
889 of the trench. Folded Ug1 and Ug2 represent two thrusting events. (c) A simplified model  
890 of a terraced hillslope formed on the front limb of a buried wedge thrust structure  
891 (modified from [Mueller and Suppe, 1997](#)). Folding events occur at times Tn, defined by  
892 onlapped sediment packages. Terraces were developed above the sediments deposited  
893 above the strata that had already been folded through an active axial surface. Limb  
894 widening by each event is denoted by Xn, which is measured parallel to bedding between  
895 outer terrace edges.

896 **Figure 12.** The fold scarp along the northeastern edge of YXL. See the location in [Figure](#)  
897 [1](#). The Qigequan Formation in the southwest of the scarp is leveled, and patchily covered  
898 by evaporites and active dunes; the playa to the northeast of the scarp is locally covered  
899 by alluviums and debris avalanches. The dashed line marks the trace of the active axial  
900 surface H. [Figures 13 a, b, c](#) and [d](#) are marked. The satellite image is sourced from  
901 Google Earth.

902 **Figure 13.** Photos and growth models of the scarp along the northeastern edge of YXL.  
903 See [Figure 12](#) for the locations of the topographic profiles and the viewpoints of the  
904 photos. (a) A horizontally-flipped photo of the scarp at the mouth of the hiking stream. (b)  
905 A topographic profile crossing the scarp close to the hiking stream. This profile shows  
906 that the scarp height at this site is ~31 m. (c) A photo of the scarp along the pipe stream.

907 The left end of the photo shows that the recent alluviums cover the northeast-dipping  
908 limb of the XSQ-YQZ anticline to form a classic growth unconformity. The angles of the  
909 folded alluviums become lower northeastwards and contact with the sediments below  
910 them in unconformity, disconformity, and conformity. (d) A topographic profile crossing  
911 the scarp near the pipe stream. This profile shows that the scarp is  $\sim 30$  m high at this site.  
912 (e) A dimensionless wide hinge zone model for changing horizon shape with increasing  
913 fractional displacement through a hinge zone with a total change in a dip of  $56^\circ$  (from  
914 [Hubert-Ferrari et al., 2007](#)). (f) Dimensionless templates of fold shapes for incrementally  
915 increasing displacement through the hinge. The hinge zone is bounded by the entry and  
916 exit axial surfaces with an arbitrary width of  $w$  (from [Hubert-Ferrari et al., 2007](#)).

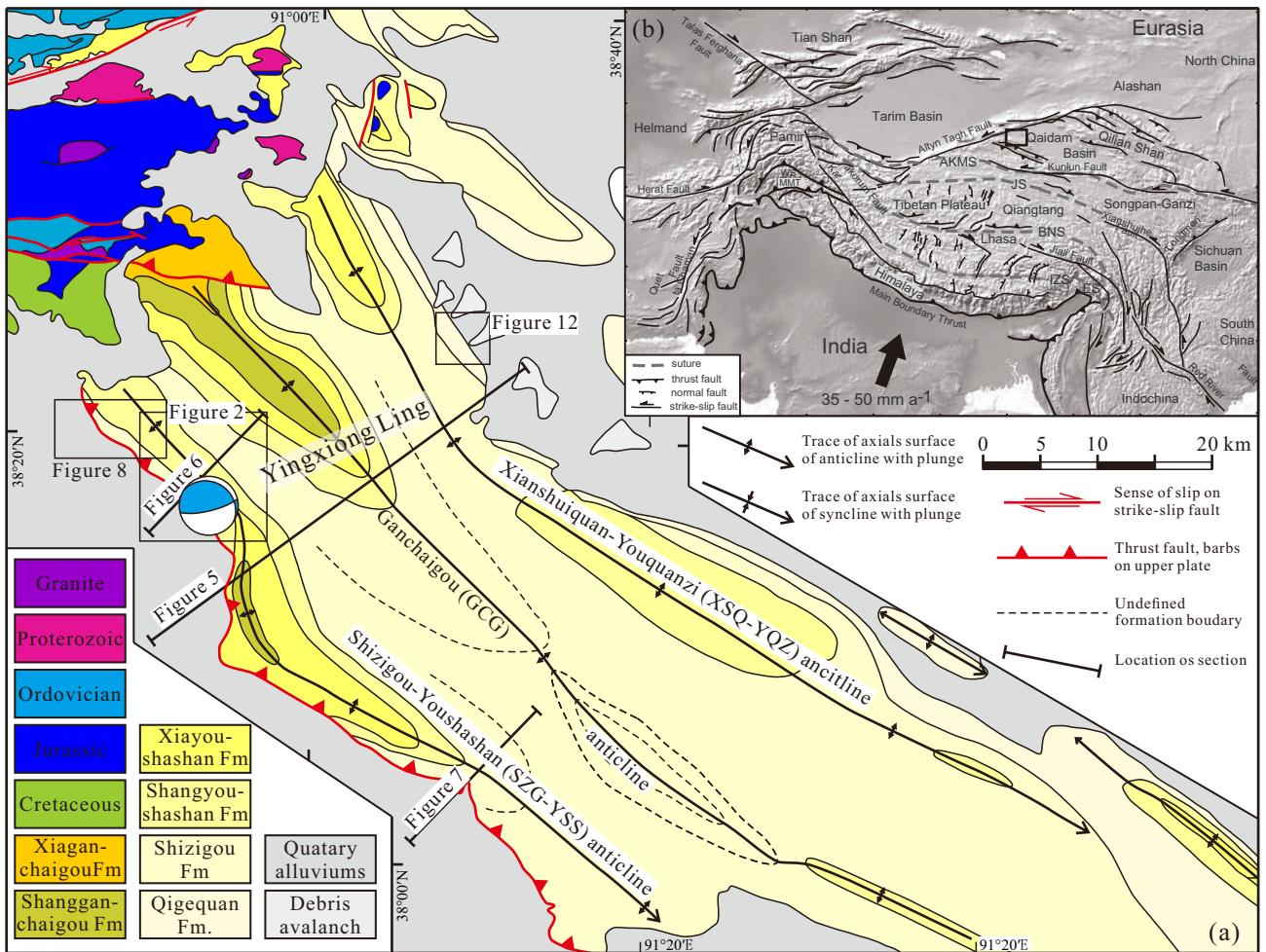


Figure 1. (a) Simplified geological map of Yingxiong Ling, southwestern Qaidam. Lower-hemisphere focal mechanisms of the March 28, 2019 Mw 5.04 Manya earthquake shows compressional quadrants in blue and dilational quadrants in clear. Locations of seismic profiles, Figures 2, 8 and 12 are marked. (b) Shaded relief map showing major fault and topographic features of the Himalayan-Tibetan orogen. The black rectangular marks the location of Figure 1a in the Himalayan-Tibetan collision system. Fault traces are from Yin & Harrison (2000), Tapponnier et al. (2001). WS, Western Himalayan Syntaxis; ES, Eastern Himalayan Syntaxis; MMT, Main Mantle Thrust; AKMS, Ayimaqin–Kunlun–Mutztagh suture; JS, Jinsha suture; BNS, Bangong–Nujiang suture; IZS, Indus–Zangbo suture.

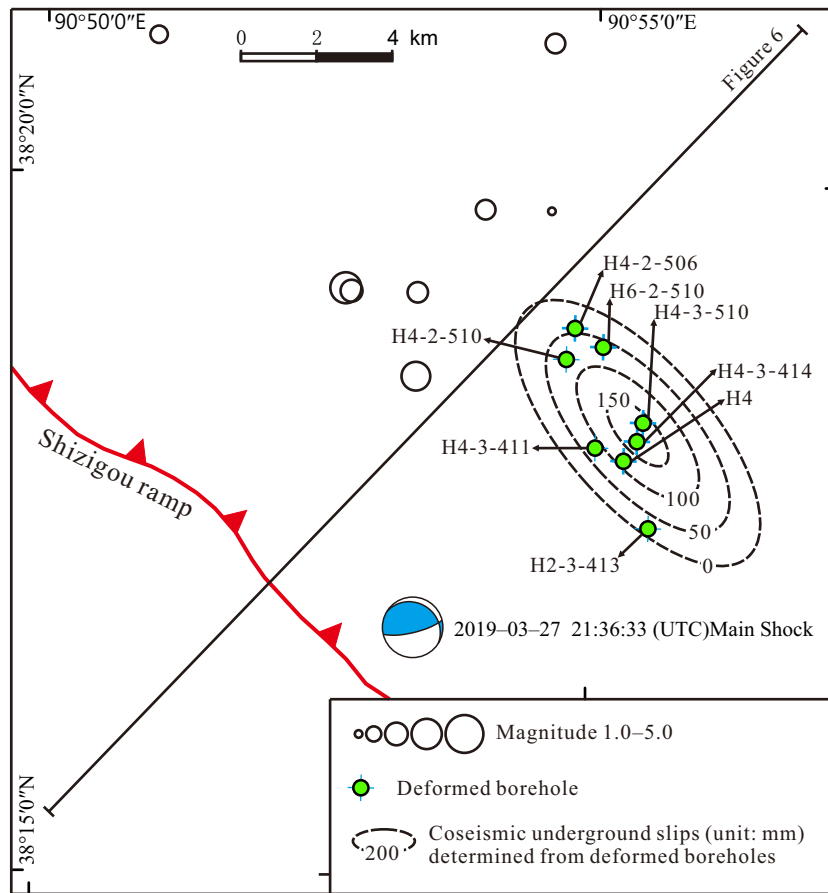


Figure 2. Coseismic slip contour map of the Shizigou (SZG) ramp on the March 28, 2019 Mw 5.04 Mangya earthquake in Yingxiong Ling. Eight damaged boreholes define the coseismic underground rupture area of the event. Epicenters of the main shock and aftershocks are from China Earthquake Data Center (2019).

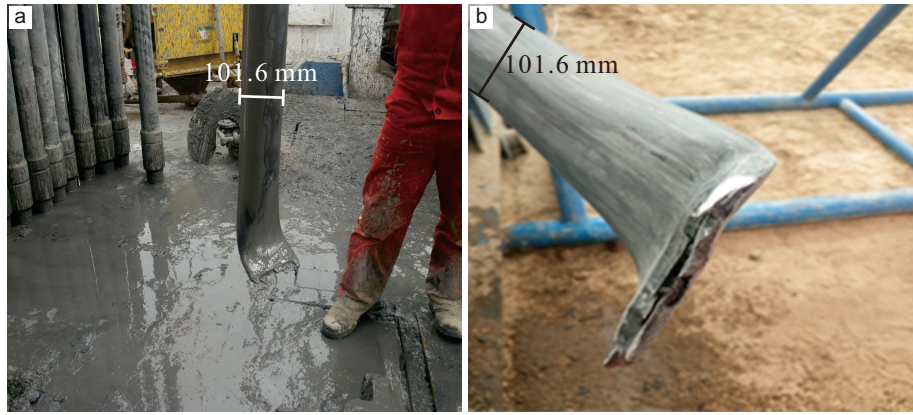


Figure 3. The offset drilling rod of borehole Shi41H4-3-414 showing that the low-angle SZG ramp cut it just at the faulting moment. Photo (a) was shot when the pipe was pulled out from the hole, and photo (b) was shot when the pipe was laid flat. The diameter of the drill pipe is 101.6 mm. See Figure 2 for the location of the borehole.

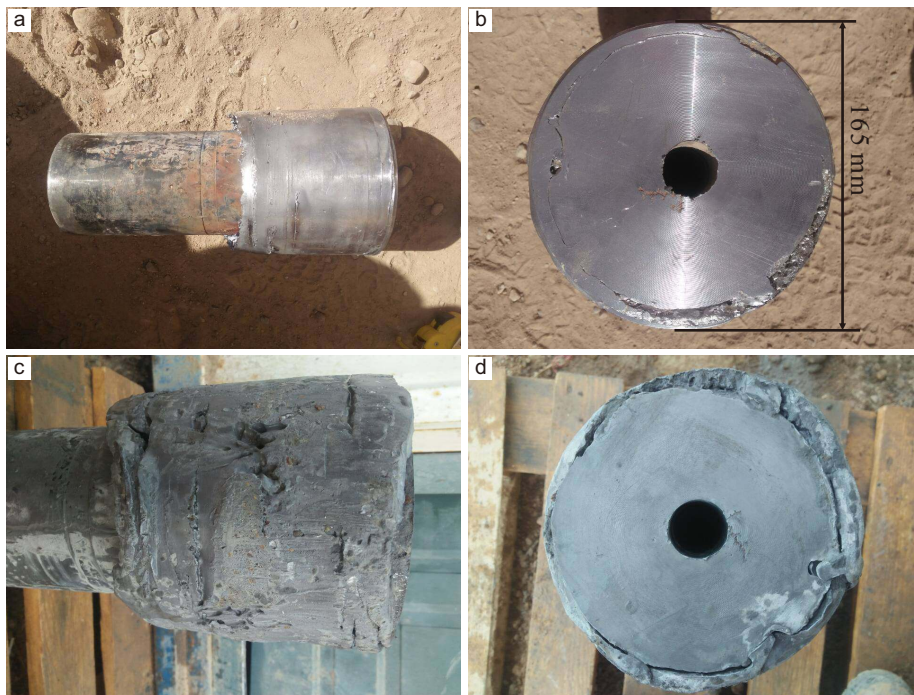


Figure 4. Photos of the lead seal before (a and b) being put into and after (c and d) being pulled out from borehole Shi41H4-3-414. The diameter of the lead seal is 165 mm and the inner diameter of the casing pipe is 172.05 mm. The side face of the lead seal has scratches, but no imprint exists in its bottom surface, which reveals that the coseismic slip at this borehole site is more than the casing pipe diameter of 196.85 mm.

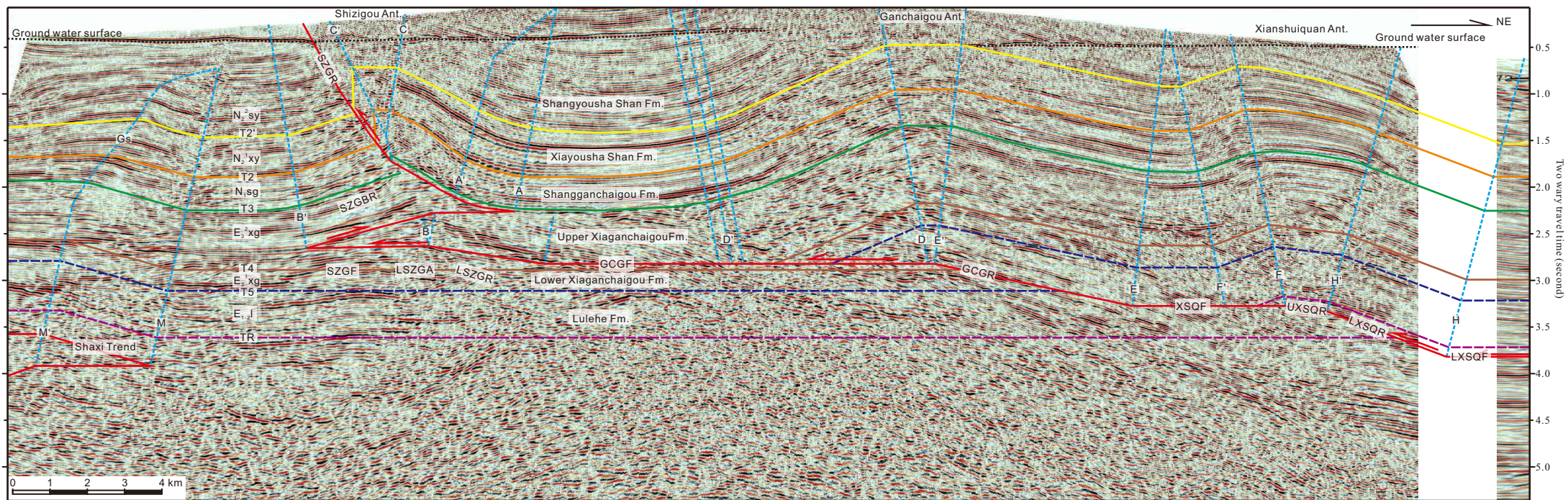


Figure 5. Interpreted seismic profile crossing the middle segment of the YXL anticlinorium. See Figure 1 for location. LSZGA, the lower Shizigou anticline; SZGR, the Shizigou ramp; SZGBR, the Shizigou back-ramp; SZGF, the Shizigou flat; LSZGR, the lower Shizigou ramp; GCGF, the Ganchaigou flat; GCGR, the Ganchaigou ramp; XSQF, the Xianshuiquan flat; UXSQR, the upper Xianshuiquan ramp; LXSQR, the lower Xianshuiquan ramp; LXSQF, the lower Xianshuiquan Flat.



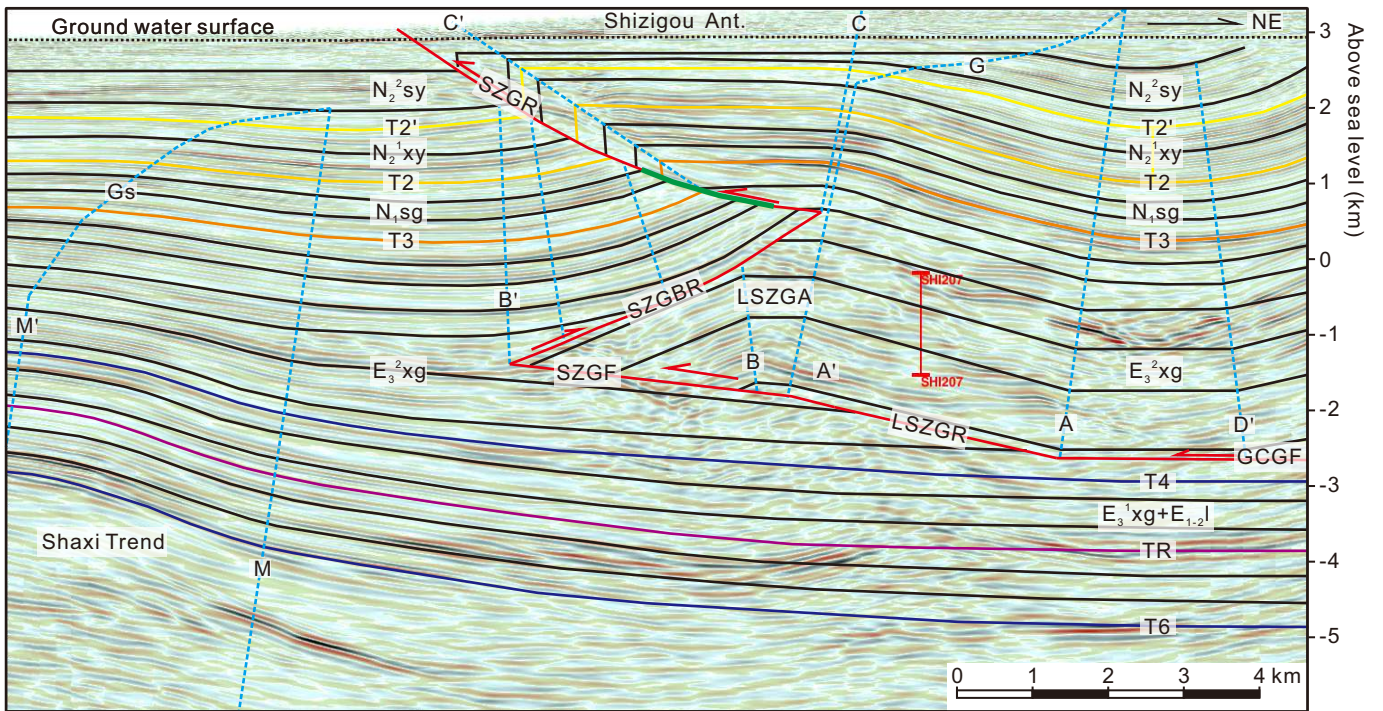


Figure 6. Interpreted seismic crossing the western SZG-YSS anticline. The green line segment on the SZG ramp is the coseismic rupture of the March 28, 2019 Mw 5.04 Mangya earthquake. The vertical scale is equal to the horizontal one. See Figure 1 for location. LSZGA, the lower Shizigou anticline; SZGR, the Shizigou ramp; SZGBR, the Shizigou back-ramp; SZGF, the Shizigou flat; LSZGR, the lower Shizigou ramp; GCGF, the Ganchaigou flat.

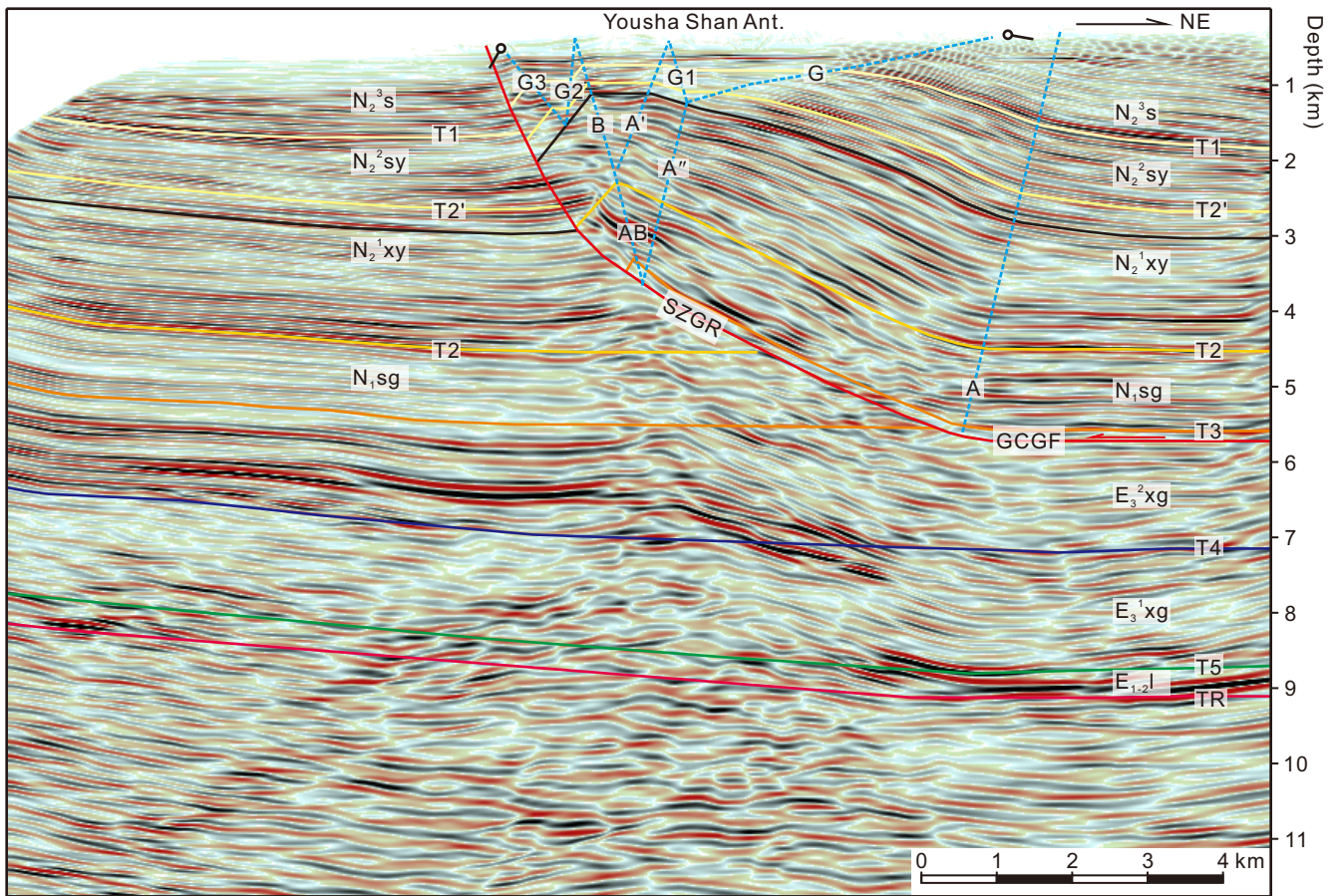


Figure 7. Interpreted seismic profile crossing the eastern segment of the SZG-YSS anticline. The vertical scale is equal to the horizontal one. See Figure 1 for location.

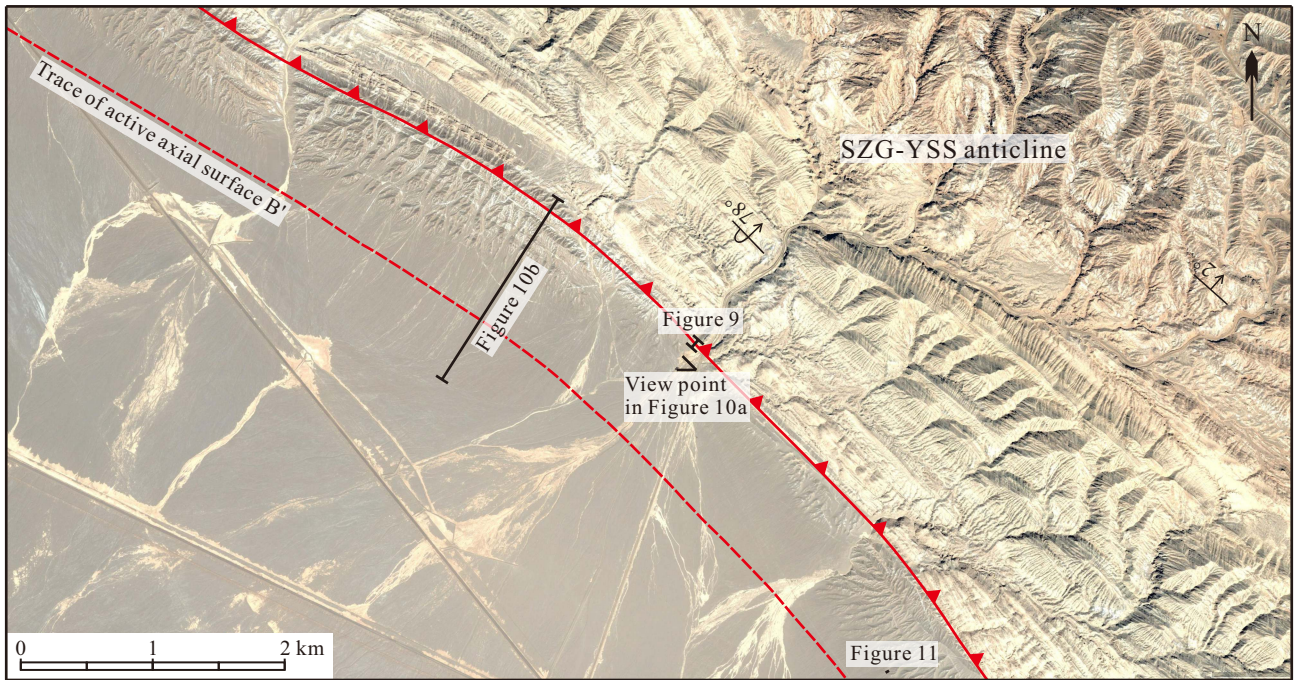


Figure 8. Folded topographic surface and fault scarp along the southwestern edge of northwestern YXL. The red solid line with bars toward the upper plate marks the SZG ramp trace; the red dashed line marks the trace of the active axial surface B'.

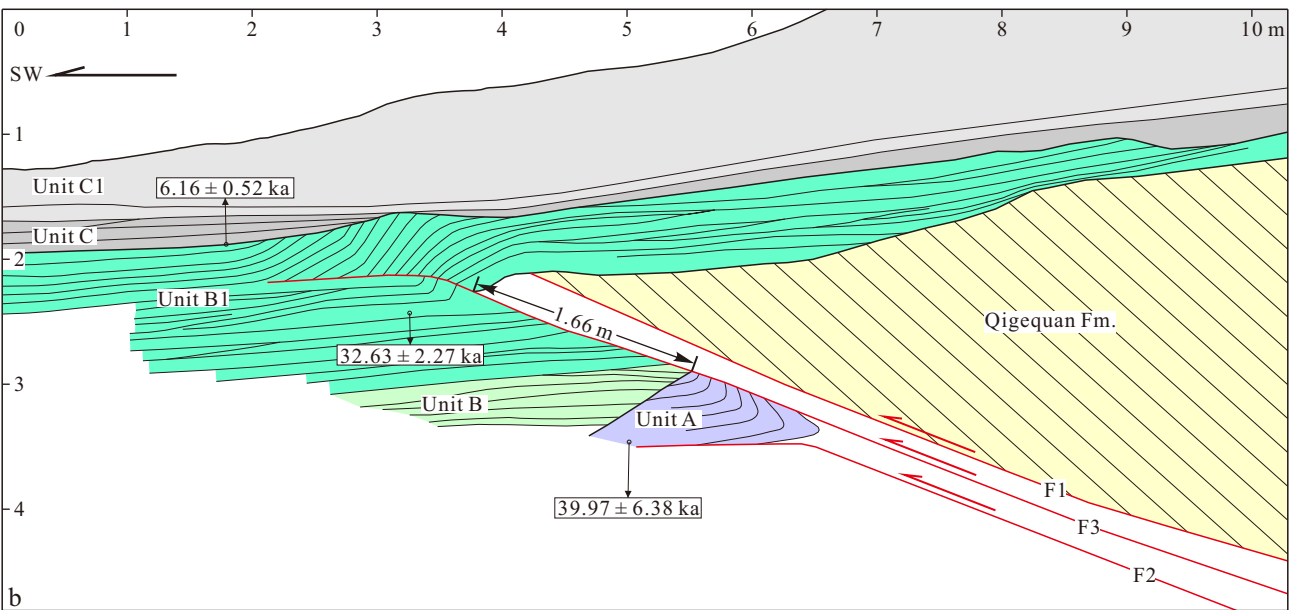
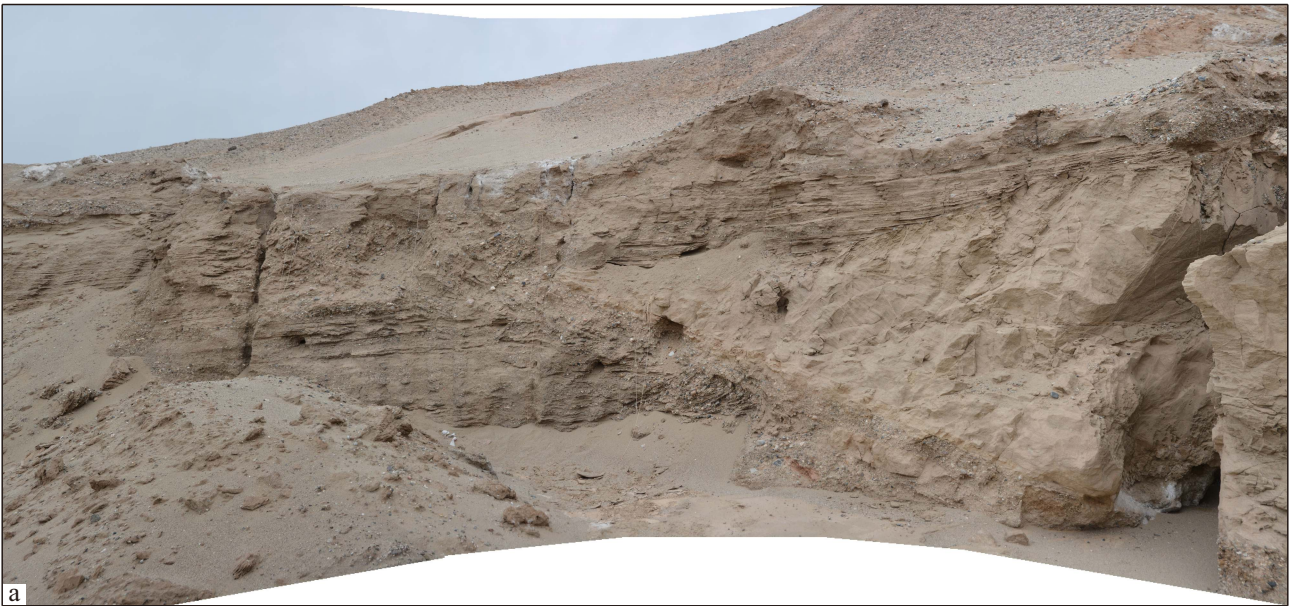


Figure 9. A outcrop photo of deformed alluviums by the SZG ramp (a) and its interpretation (b). Folding of Unit A and Unit B1 represents two thrusting events rupturing the ground surface. The event A happens between  $39.77 \pm 6.38$  ka and  $32.63 \pm 2.27$  ka, and event B1 at  $6.16 \pm 0.52$  ka. Dating results are from Xu et al. (2018a).

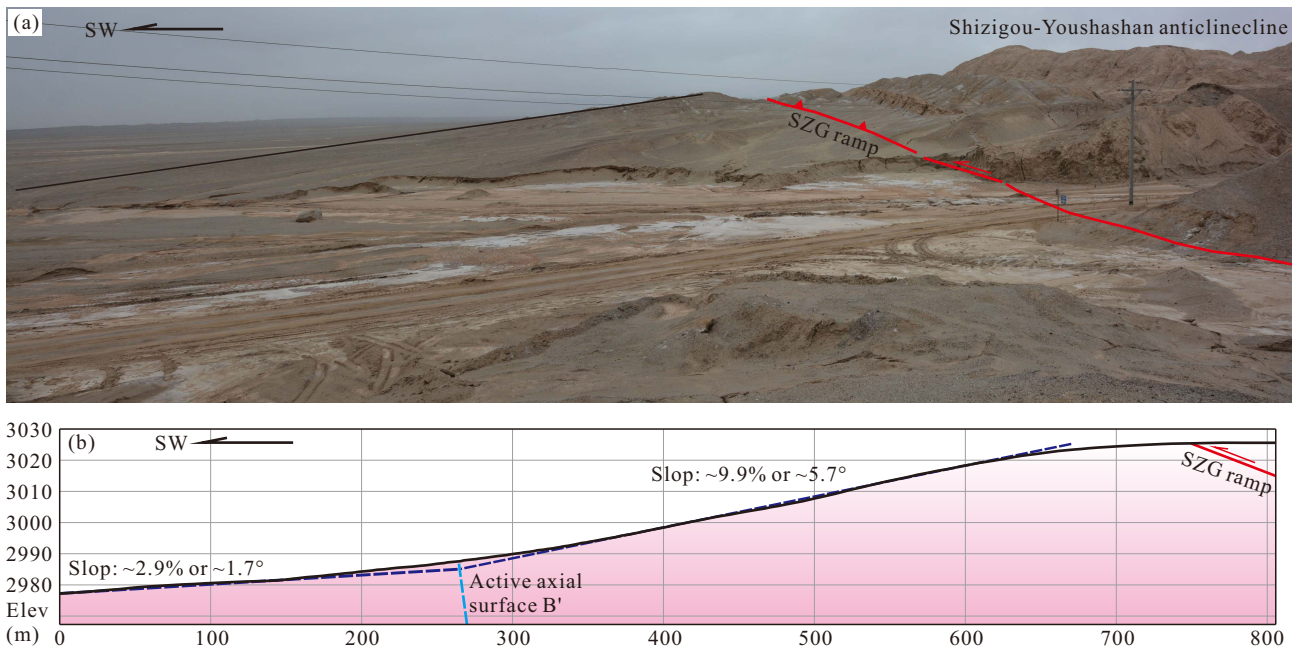


Figure 10. The folded topographic surface and the fault scarp along the southwestern edge of northwestern YXL. (a) A photo of fold scarp and fault scarp. (b) Topographic profile crossing the southwestern edge of YXL. The right side of the photo is the northwestern SZG-YSS anticline. The two topographic inflection points correspond to the outcrop of the SZG ramp and the axial surface of B', respectively.

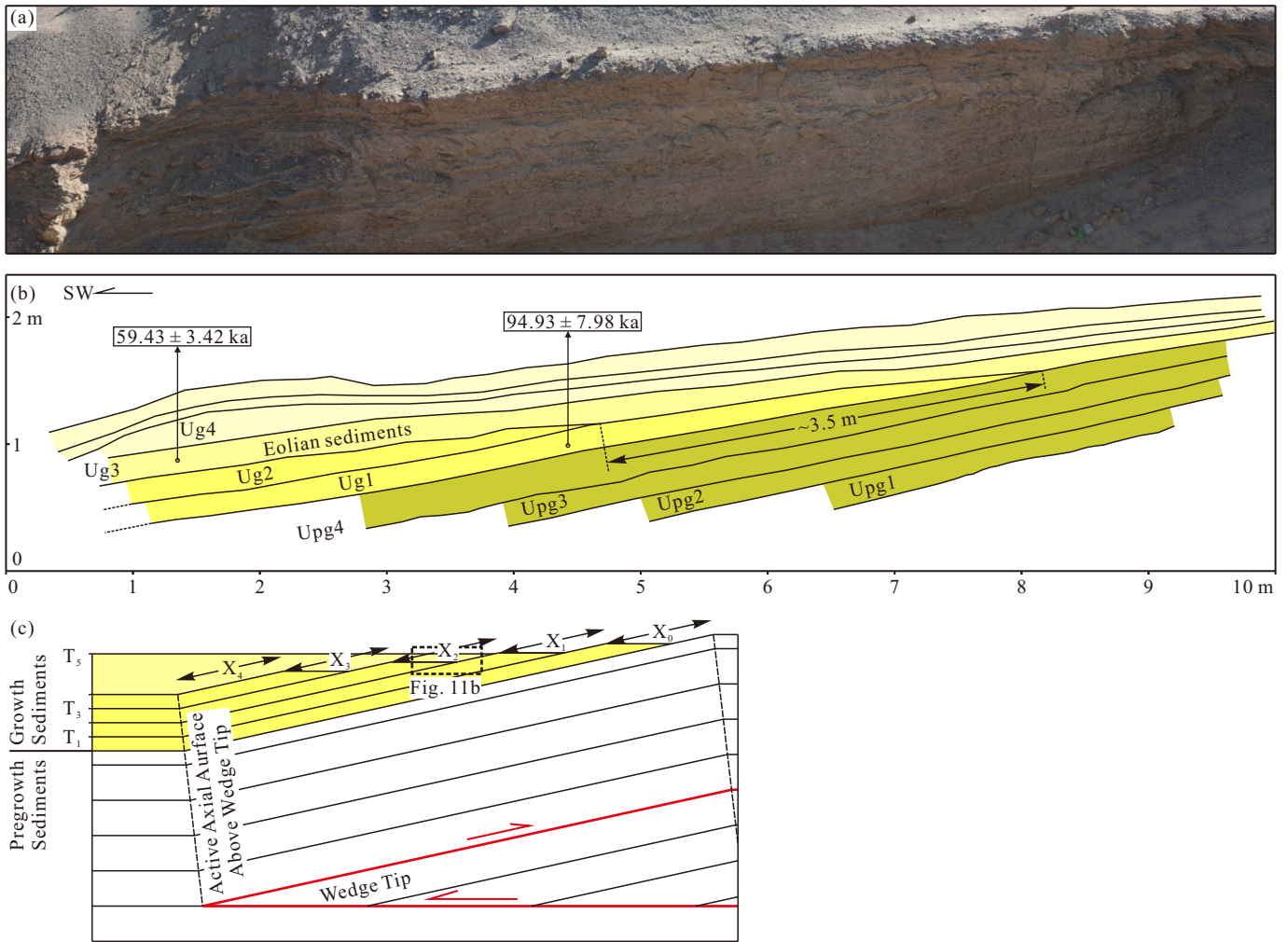


Figure 11. (a) Trench photo of folded alluvium produced by southwest-directed thrusting by the lower SZG wedge structure. (b) Reinterpretation of the trench. Folded Ug1 and Ug2 represents two thrusting events. (c) Simplified model of a terraced hillslope formed on the front limb of a buried wedge thrust structure (modified from Muller and Suppe, 1997). Folding events occur at times T<sub>n</sub>, defined by onlapped sediment packages. Terraces were developed above the sediments deposited above strata which had already been folded through an active axial surface. Limb widening by each event is denoted by X<sub>n</sub>, which is measured parallel to bedding between outer terrace edges.

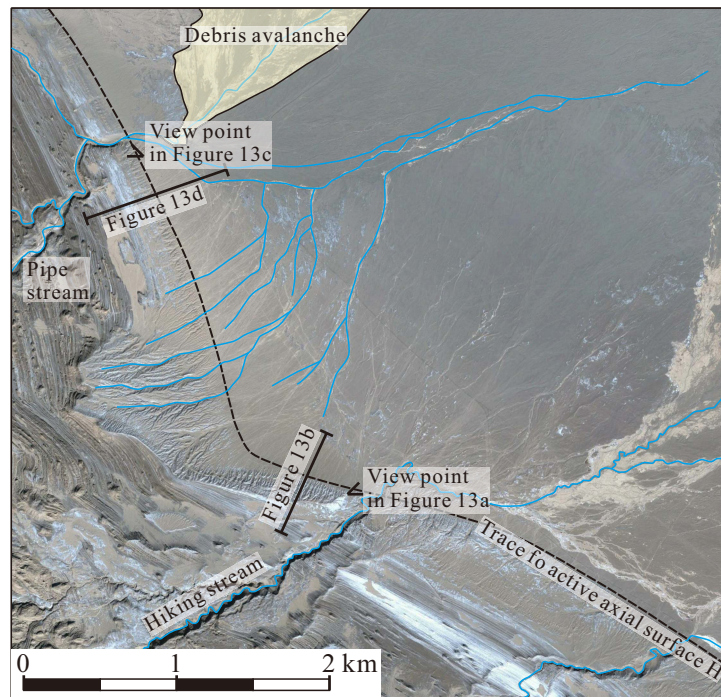


Figure 12. The fold scarp along the northeastern edge of YXL. The Qigequan Formation southwest of the scarp is leveled and patchily covered by evaporates and active sand dunes; the playa northeast of the scarp is somewhere covered by alluviums and debris avalanches. The dashed line marks the trace of trace of the active axial surface H. Figures 13 a, b, c and d are marked.

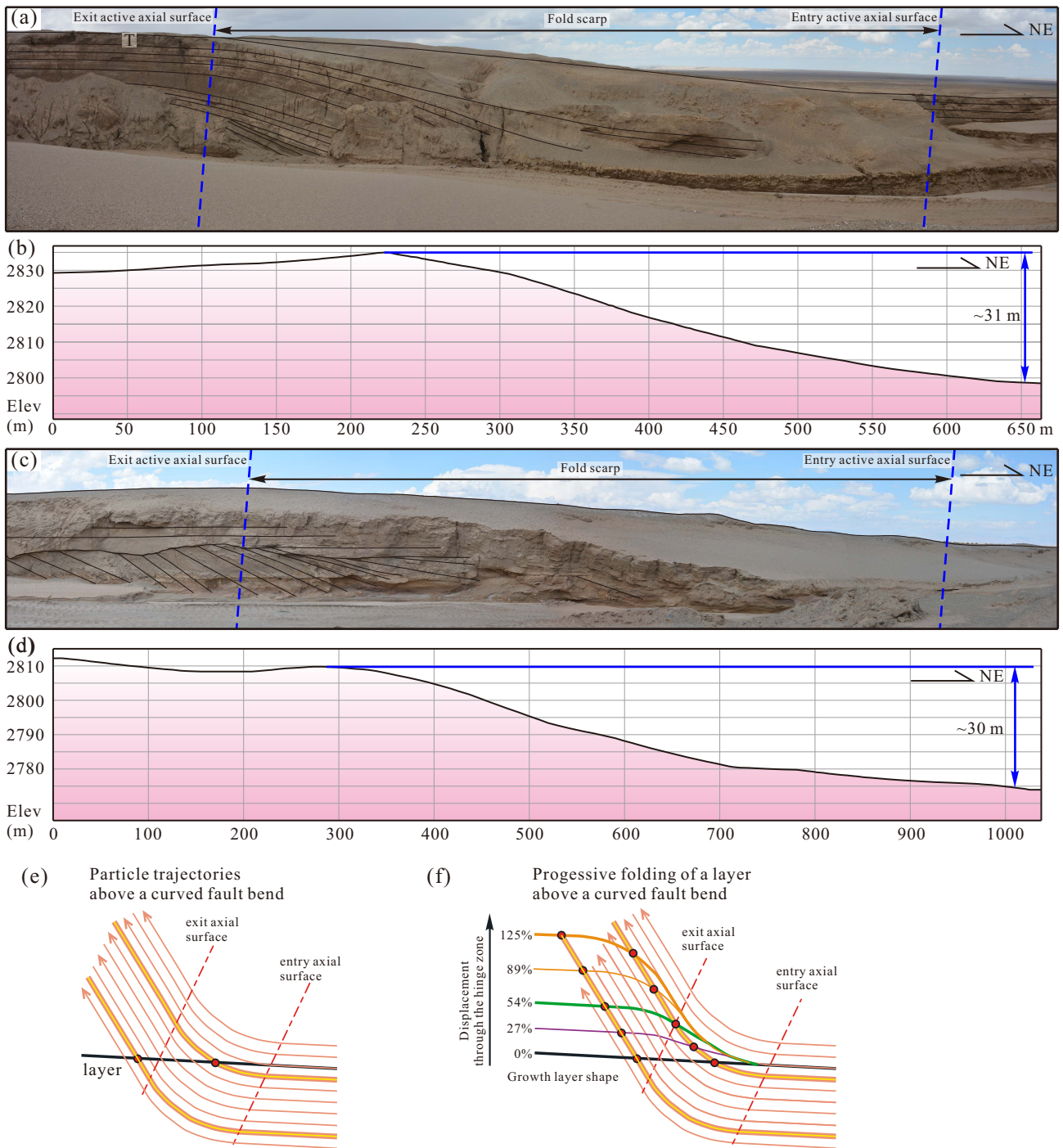


Figure 13. Photos and growth models of the scarp along the northeastern edge of YXL. See Figure 12 for locations of topographic profiles and viewpoints of photos. (a) A horizontally-flipped photo of the scarp at the mouth of the hiking stream. (b) A topographic profile crossing the scarp close to the hiking stream. This profile shows that the scarp height at this site is ~31 meters. (c) A photo of the scarp along the pipe stream. The left end of the photo shows that the recent alluviums cover the northeast-dipping limb of the XSQ-YQZ anticline to form a classic growth unconformity. The angles of the folded alluviums get lower northeastward and contact with the sediments below them in unconformity, disconformity and conformity. (d) A topographic profile crossing the scarp near the pipe stream. This profile shows that the scarp is ~30 m high at this site. (e) A dimensionless wide hinge zone model for changing horizon shape with increasing fractional displacement through a hinge zone with a total change in dip of  $56^\circ$  (from Hubert-Ferrari et al., 2007). (f) Dimensionless templates of fold shapes for incrementally increasing displacement through the hinge. Hinge zone is bounded by entry and exit axial surfaces with an arbitrary width  $w$  (from Hubert-Ferrari et al., 2007).